

Overcoming Oversmoothness in Graph Convolutional Networks via Hybrid Scattering Networks

Frederik Wenkel*, Yimeng Min*, Matthew Hirn, Michael Perlmutter[†], and Guy Wolf^{†,**}

Abstract—Geometric deep learning (GDL) has made great strides towards generalizing the design of structure-aware neural network architectures from traditional domains to non-Euclidean ones, such as graphs. This gave rise to graph neural network (GNN) models that can be applied to graph-structured datasets arising, for example, in social networks, biochemistry, and material science. Graph convolutional networks (GCNs) in particular, inspired by their Euclidean counterparts, have been successful in processing graph data by extracting structure-aware features. However, current GNN models (and GCNs in particular) are known to be constrained by various phenomena that limit their expressive power and ability to generalize to more complex graph datasets. Most models essentially rely on low-pass filtering of graph signals via local averaging operations, thus leading to oversmoothing. Here, we propose a hybrid GNN framework that combines traditional GCN filters with band-pass filters defined via the geometric scattering transform. We further introduce an attention framework that allows the model to locally attend over the combined information from different GNN filters at the node level. Our theoretical results establish the complementary benefits of the scattering filters to leverage structural information from the graph, while our experiments show the benefits of our method on various learning tasks.

Index Terms—Geometric Deep Learning, Graph Neural Networks, Geometric Scattering, Oversmoothing.



1 INTRODUCTION

DEEP learning is typically most effective when the structure of the data can be used to design the architecture of the relevant network. For example, the design of recurrent neural networks is informed by the sequential nature of time-series data. Similarly, the design of convolutional neural networks is based in part on the fact that the pixels of an image are arranged in a rectangular grid. The success of neural networks in these, as well as many other applications, has inspired the rise of geometric deep learning [1], [2], which aims to extend the success of deep learning to other forms of structured data and to develop intelligent methods for data sets that have a non-Euclidean structure.

A common approach in geometric deep learning is to model the data by a graph. In many applications, this is done by defining edges between data points that interact in a specific way, e.g., “friends” on a social network. In many other applications, one may construct a graph from a high-dimensional data set, either by defining an edge between each point and its k -nearest neighbors or by defin-

ing weighted edges via a similarity kernel. Inspired by the increasing ubiquity of graph-structured data, numerous recent works have shown graph neural networks (GNNs) to perform well in a variety of fields including biology, chemistry and social networks [3], [4], [5]. In these methods, the graph is often considered in conjunction with a set of node features, which contain “local” information about, e.g., each user of a social network.

One common family of tasks are so-called graph-level tasks, where one seeks to learn a whole-graph representation for the purposes of, e.g., predicting properties of proteins [6], [7], [8]. Another common family of tasks, which has been the primary focus of graph convolutional networks (GCNs) [5], are node-level tasks such as node classification. There, the entire data set is modeled as one large graph and the network aims to produce a useful representation of each node using both the node features and the graph structure. This work is typically conducted in the semi-supervised setting where one only knows the labels of a small fraction of the nodes.

Many popular state-of-the-art GNNs essential aim to promote similarity between adjacent nodes, which may be interpreted as a smoothing operation. While this is effective in certain settings, it can also cause a decrease in performance because of the *oversmoothing* [9] problem, where nodes become increasingly indistinguishable from one another after each subsequent layer. One promising approach for addressing this problem is the graph attention network [10], which uses attention mechanisms computed from node features to learn adaptive weighting in its message passing operations. However, this approach still fundamentally aims at enforcing similarity among neighbors, albeit in an adaptive manner.

(*) The first two authors contributed equally. (†) The last two authors jointly supervised the work. (**) Corresponding author.

F. Wenkel and G. Wolf are with Mila (Quebec Artificial Intelligence Institute) and Department of Mathematics and Statistics, University of Montreal, Montreal, QC H3T1J4 (e-mail: frederik.wenkel@umontreal.ca, guy.wolf@umontreal.ca)

Y. Min is with the Department of Computer Science, Cornell University, New York, NY 14850, USA (e-mail: min@cs.cornell.edu)

M. Hirn is with Department of Computational Mathematics, Science & Engineering, the Department of Mathematics, and the Center for Quantum Computing, Science & Engineering, Michigan State University, East Lansing, MI 48824, USA, and the Midwest Quantum Collaboratory (e-mail: mhirn@msu.edu)

M. Perlmutter is with Department of Mathematics, University of California, Los Angeles, CA 90095, USA (e-mail: perlmutter@math.ucla.edu)

Here, we propose to augment traditional GNN architectures by also including novel band-pass filters, in addition to conventional GCN-style filters¹ that essentially perform low-pass filtering [11], in order to extract richer representations for each node. This approach is based on the geometric scattering transform [12], [13], [14], whose construction is inspired by the Euclidean scattering transform introduced by Mallat in [15], and utilizes iterative cascades of graph wavelets [16], [17] and pointwise nonlinear activation functions to produce useful graph data representations.

The main contribution of this work is two hybrid GNN frameworks that utilize both traditional GCN-style filters and also novel filters based on the scattering transform. This approach is based on the following simple idea: GCN-based networks are very useful, but as they aim to enforce similarity among nodes, they essentially focus on low-frequency information. Wavelets, on the other hand, are naturally equipped to capture high-frequency information. Therefore, in a hybrid network, the different channels will capture different types of information. Such a network will therefore be more powerful than a network that only uses one style of filter or the other.

We also introduce complementary GNN modules that enhance the performance of such hybrid scattering models, including (i) the graph residual convolution, an adaptive low-pass filter that corrects high-frequency noise, and (ii) an attention framework that enables the aggregation of information from different filters individually at every node. We present theoretical results, based off of a new notion of graph structural difference, that highlight the sensitivity of scattering filters to graph regularity patterns not captured by GCN filters. Extensive empirical experiments demonstrate the ability of hybrid scattering networks for (transductive) semi-supervised node classification, to (i) alleviate oversmoothing and (ii) generalize to complex (low-homophily) datasets. Moreover, we also present empirical evidence that our framework translates well to inductive graph-level tasks.

The remainder of this paper is organized as follows. We review related work on GNN models and geometric scattering in Sec. 2 and introduce important concepts that will be used throughout this work in Sec. 3. We then formulate the hybrid scattering network in Sec. 4, followed by a theoretical study of the benefits of such models in Sec. 5. In Sec. 6, we present empirical results before concluding in Sec. 7.

2 RELATED WORK

Theoretical analyses [9], [11] of GCN and related models show that they may be viewed as Laplacian smoothing operations and, from the signal processing perspective, essentially perform low-pass filters on the graph features. One approach towards addressing this problem is the graph attention network proposed by [10], which uses self-attention mechanisms to address these shortcomings by adaptively reweighting local neighborhoods. In [18], the authors construct a low-rank approximation of the graph Laplacian that

1. Throughout this text, we will use the term GCN to refer to the network introduced by Kipf and Welling in [5]. We will use the term GNN to refer to graph neural networks (spectral, convolutional, or otherwise) in general.

efficiently gathers multi-scale information and demonstrate the effectiveness of their method on citation networks and the QM8 quantum chemistry dataset. In [19], the authors take an approach similar to GCN, but use multiple powers of the adjacency matrix to learn higher-order neighborhood information. Finally, in [20] the authors used graph wavelets to extract higher-order neighborhood.

In addition to the learned networks discussed above, several works [12], [13], [14] have introduced different variations of the graph scattering transform. These papers aim to extend the Euclidean scattering transform of Mallat [15] to graph-structured data and propose predesigned, wavelet-based networks. In [12], [14], [21], [22], extensive theoretical studies of these networks show that they have desirable stability, invariance, and conservation of energy properties. The practical utility of these networks has been established in [13], which primarily focuses on graph classification, and in [23], [24], [25], which used the graph scattering transform to generate molecules. Building off of these results, which use handcrafted formulations of the scattering transform, recent work [26] has proposed a framework for a data-driven tuning of the traditionally handcrafted geometric scattering design that maintains the theoretical properties from traditional designs, while also showing strong empirical results in whole-graph settings.

3 GEOMETRIC DEEP LEARNING BACKGROUND

3.1 Graph Signal Processing

Let $G = (V, E, w)$ be a weighted graph, characterized by a set of nodes (also called vertices) $V := \{v_1, \dots, v_n\}$, a set of undirected edges $E \subseteq V \times V$, and a function $w : E \rightarrow (0, \infty)$ assigning positive edge weights to the edges. Let $\mathbf{X} \in \mathbb{R}^{n \times d_x}$ be a *node features matrix*. We shall interpret the i^{th} row of \mathbf{X} as representing the features of the node v_i , and therefore, we shall denote these rows by $\mathbf{X}[v_i] \in \mathbb{R}^{1 \times d_x}$. The columns of \mathbf{X} , on the other hand, will be denoted by \mathbf{x}_i . Each of these columns may be naturally identified with a *graph signal*, i.e., a function $x_i : V \rightarrow \mathbb{R}$, $x_i(v_j) := \mathbf{x}_i[j]$. In what follows, for simplicity, we will not distinguish between the vectors \mathbf{x}_i and the functions x_i and will refer to both as graph signals.

We define the weighted *adjacency matrix* $\mathbf{W} \in \mathbb{R}^{n \times n}$ of G by $\mathbf{W}[v_i, v_j] := w(v_i, v_j)$ if $\{v_i, v_j\} \in E$, and set all other entries to zero. We further define the *degree matrix* $\mathbf{D} \in \mathbb{R}^{n \times n}$ as the diagonal matrix $\mathbf{D} := \text{diag}(\deg(v_1), \dots, \deg(v_n))$ with each diagonal element $\deg(v_i) := \sum_{j=1}^n \mathbf{W}[v_i, v_j]$ being the *degree* of a node v_i . In the following, we will also use the shorthand d_{v_i} to denote the degree of v_i . We consider the *combinatorial graph Laplacian* matrix $\mathbf{L} := \mathbf{D} - \mathbf{W}$ and the *symmetric normalized Laplacian* given by

$$\mathcal{L} := \mathbf{D}^{-1/2} \mathbf{L} \mathbf{D}^{-1/2} = \mathbf{I}_n - \mathbf{D}^{-1/2} \mathbf{W} \mathbf{D}^{-1/2}.$$

It is well known that this matrix is symmetric, positive semi-definite, and admits an orthonormal basis of eigenvectors such that $\mathcal{L} \mathbf{q}_i = \lambda_i \mathbf{q}_i$. Therefore, we may write

$$\mathcal{L} = \mathbf{Q} \mathbf{\Lambda} \mathbf{Q}^T = \sum_{i=1}^n \lambda_i \mathbf{q}_i \mathbf{q}_i^T,$$

where $\mathbf{\Lambda} := \text{diag}(\lambda_1, \dots, \lambda_n)$ and \mathbf{Q} is the orthogonal matrix whose i -th column is \mathbf{q}_i .

We will use the eigendecomposition of \mathcal{L} to define the *graph Fourier transform*, with the eigenvectors $\mathbf{q}_1, \dots, \mathbf{q}_n$ being interpreted as Fourier modes. The notion of oscillation on irregular domains like graphs is delicate, but can be reframed in terms of increasing variation of the modes, with the eigenvalues $0 = \lambda_1 \leq \lambda_2 \leq \dots \leq \lambda_n \leq 2$ interpreted as (squared) frequencies.² The *Fourier transform* of a graph signal $\mathbf{x} \in \mathbb{R}^n$ is defined by $\hat{\mathbf{x}}[i] := \langle \mathbf{x}, \mathbf{q}_i \rangle$ for $1 \leq i \leq n$ and the inverse Fourier transform may be computed by $\mathbf{x} = \sum_{i=1}^n \hat{\mathbf{x}}[i] \mathbf{q}_i$. It will frequently be convenient to write these equations in matrix form as $\hat{\mathbf{x}} = \mathbf{Q}^T \mathbf{x}$ and $\mathbf{x} = \mathbf{Q} \hat{\mathbf{x}}$.

We recall that in the Euclidean setting, the convolution of two signals in the spatial domain corresponds to the pointwise multiplication of their Fourier transforms. Therefore, we may define the convolution of a signal \mathbf{x} with a filter \mathbf{g} by the rule that $\mathbf{g} \star \mathbf{x}$ is the unique vector such that $(\mathbf{g} \star \mathbf{x})[i] = \hat{\mathbf{g}}[i] \hat{\mathbf{x}}[i]$ for $1 \leq i \leq n$. Applying the inverse Fourier transform, one may verify that

$$\mathbf{g} \star \mathbf{x} = \sum_{i=1}^n \hat{\mathbf{g}}[i] \hat{\mathbf{x}}[i] \mathbf{q}_i = \sum_{i=1}^n \hat{\mathbf{g}}[i] \mathbf{q}_i \mathbf{q}_i^T \mathbf{x} = \mathbf{Q} \hat{\mathbf{G}} \mathbf{Q}^T \mathbf{x}, \quad (1)$$

where $\hat{\mathbf{G}} := \text{diag}(\hat{\mathbf{g}}) = \text{diag}(\hat{\mathbf{g}}[1], \dots, \hat{\mathbf{g}}[n])$. Hence, convolutional graph filters can be parameterized by considering the Fourier coefficients in $\hat{\mathbf{G}}$.

3.2 Spectral Graph Neural Network Constructions

A *graph filter* is a function $F : \mathbb{R}^{n \times d_x} \rightarrow \mathbb{R}^{n \times d_y}$ that transforms a node feature matrix $\mathbf{X} \in \mathbb{R}^{n \times d_x}$ into a new feature matrix $\mathbf{Y} \in \mathbb{R}^{n \times d_y}$. GNNs typically feature several layers each of which produces a new set of features by filtering the output of the previous layer. We will usually let \mathbf{X}^0 denote the initial node feature matrix, which is the input to the network and let \mathbf{X}^ℓ denote the node feature matrix after the ℓ -th layer.

In light of Eq. 1, a natural way to construct learned graph filters would be to directly learn the Fourier coefficients in $\hat{\mathbf{g}}$. Indeed this was the approach used in the pioneering work of Bruna et al. [27]. However, this approach has several drawbacks. First, it results in n learnable parameters in each convolutional filter. Therefore, a network using such filters would not scale well to large data sets due to the computational cost. At the same time, such filters are not necessarily well-localized in space and are prone to overfitting [28]. Moreover, networks of the form introduced in [27] typically cannot be generalized to different graphs [1]. However, recent work [29] has shown that this latter issue can be overcome by formulating the Fourier coefficients $\hat{\mathbf{g}}[i]$ as smooth functions of the Laplacian eigenvalues λ_i , $1 \leq i \leq n$. In particular, this will be the case for the filters used in the networks considered in this work.

A common approach (e.g., used in [5], [18], [28], [30], [31]) to formulate such filters is by using polynomials of the Laplacian eigenvalues to set $\hat{\mathbf{g}}[i] := \sum_{j=0}^k \theta_j \lambda_i^j$ (or equivalently $\hat{\mathbf{G}} = \sum_{j=0}^k \theta_j \Lambda^j$) for some $k \ll n$. It can be verified [28] that this approach yields convolutional filters that are k -localized in space and that can be written as

² This interpretation originates from motivating the graph Fourier transform via the combinatorial graph Laplacian $\mathbf{L} = \sum_{i=1}^n \tilde{\lambda}_i \tilde{\mathbf{q}}_i \tilde{\mathbf{q}}_i^T$ with $\tilde{\lambda}_i = \tilde{\mathbf{q}}_i^T \mathbf{L} \tilde{\mathbf{q}}_i = \sum_{j=1}^n \mathbf{W}[i, j] (\tilde{\mathbf{q}}_i[j] - \tilde{\mathbf{q}}_j[j])^2$ the variation of $\tilde{\mathbf{q}}_i$.

$\mathbf{g}_\theta \star \mathbf{x} = \sum_{j=0}^k \theta_j \mathcal{L}^j \mathbf{x}$. This reduces the number of trainable parameters in each filter from n to $k+1$ and allows one to perform convolution without explicitly computing the spectral decomposition of the Laplacian, which is expensive for large graphs.

One particularly noteworthy network that uses this method is [28], which writes the filters in terms of the Chebyshev polynomials defined by $T_0(x) = 1$, $T_1(x) = x$ and $T_j(x) := 2xT_{j-1}(x) - T_{j-2}(x)$. They first renormalize the eigenvalue matrix $\tilde{\Lambda} := 2\mathbf{L}/\lambda_n - \mathbf{I}_n$ and then define $\hat{\mathbf{G}} := \sum_{j=0}^k \theta_j T_j(\tilde{\Lambda})$. This gives rise to a k -localized filtering operation of the form

$$\mathbf{g}_\theta \star \mathbf{x} = \sum_{j=0}^k \theta_j T_j(\tilde{\mathcal{L}}), \quad (2)$$

where $\tilde{\mathcal{L}} := 2\mathcal{L}/\lambda_n - \mathbf{I}_n$.

3.3 Graph Convolutional Networks

One of the most widely used GNNs is the Graph Convolutional Network (GCN) [5]. This network is derived from the Chebyshev construction [28] mentioned above by setting $k = 1$ in Eq. 2 and approximating $\lambda_n \approx 2$, which yields

$$\begin{aligned} \mathbf{g}_{\theta_0, \theta_1} \star \mathbf{x} &\approx \theta_0 \mathbf{x} + \theta_1 (\mathcal{L} - \mathbf{I}_n) \mathbf{x} \\ &= \theta_0 \mathbf{x} - \theta_1 \mathbf{D}^{-1/2} \mathbf{W} \mathbf{D}^{-1/2} \mathbf{x}. \end{aligned}$$

To further reduce the number of trainable parameters, the authors then set $\theta := \theta_0 = -\theta_1$. The resulting convolutional filter has the form

$$\mathbf{g}_\theta \star \mathbf{x} = \theta \left(\mathbf{I}_n + \mathbf{D}^{-1/2} \mathbf{W} \mathbf{D}^{-1/2} \right) \mathbf{x}. \quad (3)$$

One may verify that $\mathbf{I}_n + \mathbf{D}^{-1/2} \mathbf{W} \mathbf{D}^{-1/2} = 2\mathbf{I}_n - \mathcal{L}$, and therefore, Eq. 3 essentially corresponds to setting $\hat{\mathbf{g}}[i] := \theta(2 - \lambda_i)$ in Eq. 1. The eigenvalues of $\mathbf{I}_n + \mathbf{D}^{-1/2} \mathbf{W} \mathbf{D}^{-1/2}$ take values in $[0, 2]$. Thus, to avoid vanishing or exploding gradients, the authors use a renormalization trick

$$\mathbf{I}_n + \mathbf{D}^{-1/2} \mathbf{W} \mathbf{D}^{-1/2} \rightarrow \tilde{\mathbf{D}}^{-1/2} \tilde{\mathbf{W}} \tilde{\mathbf{D}}^{-1/2}, \quad (4)$$

where $\tilde{\mathbf{W}} := \mathbf{I}_n + \mathbf{W}$ and $\tilde{\mathbf{D}}$ is a diagonal matrix with $\tilde{\mathbf{D}}[v_i, v_i] := \sum_{j=1}^n \tilde{\mathbf{W}}[v_i, v_j]$ for $i \in [n]$. Setting $\mathbf{A} := \tilde{\mathbf{D}}^{-1/2} \tilde{\mathbf{W}} \tilde{\mathbf{D}}^{-1/2}$, and using multiple channels we obtain a layer-wise propagation rule of the form $\mathbf{x}_j^\ell = \sigma \left(\sum_{i=1}^{N_{\ell-1}} \theta_{ij}^\ell \mathbf{A} \mathbf{x}_i^{\ell-1} \right)$, where N_ℓ is the number of channels used in the ℓ -th layer and $\sigma(\cdot)$ is an elementwise nonlinearity. In matrix form we write

$$\mathbf{X}^\ell = F_{\text{gcN}} \left(\mathbf{X}^{\ell-1} \right) = \sigma \left(\mathbf{A} \mathbf{X}^{\ell-1} \Theta^\ell \right). \quad (5)$$

We interpret the matrix \mathbf{A} as computing a localized average of each channel $\mathbf{x}_i^{\ell-1}$ around each mode and the matrix Θ as sharing information across channels. This filter can also be observed at the node level as

$$\mathbf{X}^\ell[v] = \sigma \left(\sum_{w \in \mathcal{N}_v} \frac{1}{\sqrt{(d_v+1)(d_w+1)}} \mathbf{X}^{\ell-1}[w] \Theta^\ell \right),$$

where \mathcal{N}_v denotes the one-step neighborhood of node v and $\mathcal{N}_{\underline{v}} := \mathcal{N}_v \cup \{v\}$. This process can be split into three steps:

$$\mathbf{X}_a^\ell[w] = \mathbf{X}^{\ell-1}[w] \Theta^\ell \text{ for all } w \in \mathcal{N}_{\underline{v}} \quad (6a)$$

$$\mathbf{X}_b^\ell[v] = \sum_{w \in \mathcal{N}_{\underline{v}}} \frac{1}{\sqrt{(d_v+1)(d_w+1)}} \mathbf{X}_a^\ell[w] \quad (6b)$$

$$\mathbf{X}_c^\ell[v] = \sigma(\mathbf{X}_b^\ell[v]), \quad (6c)$$

which we refer to as the *transformation* step (Eq. 6a), the *aggregation* step (Eq. 6b) and the *activation* step (Eq. 6c).

As discussed earlier, the GCN filter described above may be viewed as a low-pass filter that suppresses high-frequency information. For simplicity, we focus on the convolution in Eq. 3 before the renormalization. This convolution essentially corresponds to pointwise Fourier multiplication by $\hat{\mathbf{g}}[i] = \theta(2 - \lambda_i)$, which is strictly decreasing in λ_i . Therefore, repeated applications of this filter effectively zero-out the higher frequencies. This is consistent with the oversmoothing problem discussed in [9].

3.4 Graph Attention Networks

Another popular network that is widely used for node classification tasks is the graph attention network (GAT) [10], which uses an attention mechanism to guide and adjust the aggregation of features from adjacent nodes. First, the node features $\mathbf{X}^{\ell-1}$ are linearly transformed to $\bar{\mathbf{X}}^\ell := \mathbf{X}^{\ell-1} \Theta$ using a learned weight matrix $\Theta \in \mathbb{R}^{d \times d'}$. Then, the aggregation coefficients are learned via

$$\alpha_{v \leftarrow u} = \frac{\exp(\text{LeakyReLU}(\left[\bar{\mathbf{X}}^\ell[v] \parallel \bar{\mathbf{X}}^\ell[u] \right] \mathbf{a}))}{\sum_{w \in \mathcal{N}_{\underline{v}}} \exp(\text{LeakyReLU}(\left[\bar{\mathbf{X}}^\ell[v] \parallel \bar{\mathbf{X}}^\ell[w] \right] \mathbf{a}))},$$

where $\mathbf{a} \in \mathbb{R}^{2d'}$ is a shared attention vector and \parallel denotes horizontal concatenation. The output feature corresponding to a single attention head is given by $\mathbf{X}^\ell[v] = \sigma(\sum_{u \in \mathcal{N}_v} \alpha_{v \leftarrow u} \bar{\mathbf{X}}^\ell[u])$. To increase the expressivity of this network, the authors then use a multi-headed attention mechanism, with Γ heads, to generate concatenated features

$$\mathbf{X}^\ell[v] = \parallel_{\gamma=1}^\Gamma \sigma \left(\sum_{u \in \mathcal{N}_{\underline{v}}} \alpha_{v \leftarrow u}^\gamma \bar{\mathbf{X}}_\gamma^\ell[u] \right). \quad (7)$$

3.5 Challenges in Geometric Deep Learning

Many GNN models, including GCN [5] and GAT [10], are subject to the so-called *oversmoothing* problem [9], caused by aggregation steps (such as Eq. 6b) that essentially consist of localized averaging operations. As discussed in Sec. 3.3 and also [11], from a signal processing point of view, this corresponds to a *low-pass filtering* of graph signals. Moreover, as discussed in [32], these networks are also subject to *underreaching* [32]. Most GNNs (including GCN and GAT) can only relate information from nodes within a distance equal to the number of GNN layers, and because of the oversmoothing problem, they typically use a small number of layers in practice. Therefore, the oversmoothing and underreaching problem combine to significantly limit the ability of GNNs to capture long-range dependencies. In Sec. 4, we will introduce a hybrid network, which aims to address these challenges by using both GCN-style channels and channels based on the geometric scattering transform discussed below.

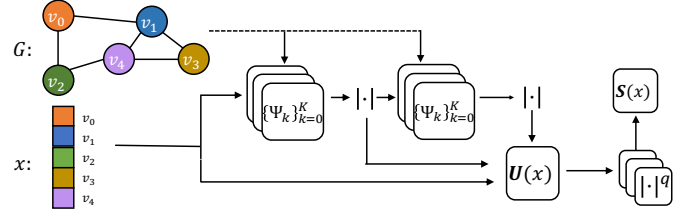


Fig. 1. Illustration of two-layer geom. scattering at the node level ($\mathbf{U}(\mathbf{x}) = \{\mathbf{U}_p \mathbf{x} : p \in \mathbb{N}_0^m, m = 0, 1, 2\}$) and at the graph level ($\mathbf{S}(\mathbf{x}) = \{\mathbf{S}_{p,q} \mathbf{x} : q \in \mathbb{N}, p \in \mathbb{N}_0^m, m = 0, 1, 2\}$), extracted according to the wavelet cascade in Eqs. 9-11.

3.6 Geometric Scattering

In this section, we review the geometric scattering transform constructed in [13] for graph classification and show how it may be adapted for node-level tasks. As we shall see, this node-level geometric scattering will address the challenges discussed above in Sec. 3.5, by using band-pass filters that capture high-frequency information and have wider receptive fields.

The geometric scattering transform uses wavelets based upon raising the *lazy random walk* matrix

$$\mathbf{P} := \frac{1}{2}(\mathbf{I}_n + \mathbf{W}\mathbf{D}^{-1}),$$

to dyadic powers 2^j , which can be interpreted as differing degrees of resolution. Entrywise, we note that

$$(\mathbf{P}\mathbf{X})[v] = \frac{1}{2}\mathbf{X}[v] + \frac{1}{2}\sum_{w \in \mathcal{N}_v} d_w^{-1}\mathbf{X}[w]. \quad (8)$$

Thus, \mathbf{P} may be viewed as a localized averaging operation operator analogous to those used in, e.g., GCN, and the powers \mathbf{P}^{2^j} may be viewed as low-pass filters which suppress high-frequencies. In order to better retain this high-frequency information, we define multiscale *graph diffusion wavelets* by subtracting these low-pass filters at different scales [17]. Specifically, for $k \in \mathbb{N}_0$, we define a wavelet $\Psi_k \in \mathbb{R}^{n \times n}$ at scale 2^k by

$$\Psi_0 := \mathbf{I}_n - \mathbf{P}, \quad \Psi_k := \mathbf{P}^{2^{k-1}} - \mathbf{P}^{2^k}, \quad k \geq 1. \quad (9)$$

From a frequency perspective, we may interpret each Ψ_k as capturing information at a different frequency band. From a spatial perspective, we may view Ψ_k as encoding information on how a 2^k -step neighborhood differs from a smaller 2^{k-1} -step one. Such wavelets are usually organized in a filter bank $\{\Psi_k, \Phi_K\}_{0 \leq k \leq K}$, along with a low-pass filter $\Phi_K := \mathbf{P}^{2^K}$. One should note that these wavelets are not self-adjoint operators on the standard \mathbf{L}^2 space. However, it was shown in [22] that this wavelet filter bank is a self-adjoint non-expansive frame on a suitably weighted inner-product space.

The geometric scattering transform is a multi-layered architecture that iteratively applies wavelet convolutions and nonlinear activation functions in an alternating cascade as illustrated in Fig. 1. It is parameterized by paths $p := (k_1, \dots, k_m)$. Formally, we define

$$\mathbf{U}_p \mathbf{x} := \Psi_{k_m} \circ \sigma \circ \Psi_{k_{m-1}} \cdots \sigma \circ \Psi_{k_2} \circ \sigma \circ \Psi_{k_1} \mathbf{x} \quad (10)$$

where σ is a nonlinear activation function.³ We note that the nonlinearity σ might vary in each step of the cascade. However, we will suppress this possible dependence to avoid cumbersome notation. We also note that in our theoretical results, if we assume, for example, that σ is strictly increasing, this assumption is intended to apply to all nonlinearities used in the cascade. In our experiments, we use the absolute value, i.e., $\sigma(\mathbf{x}[v_i]) = |\mathbf{x}[v_i]|$.

When applied in the context of graph-classification, the scattering features are frequently aggregated by taking q^{th} -order moments,

$$S_{p,q}\mathbf{x} := \sum_{i=1}^n |(U_p \mathbf{x})[v_i]|^q. \quad (11)$$

However, since our current focus is on node-level tasks we will not use these moments here.

The original formulations of geometric scattering were fully designed networks without any learned convolutions between channels. Here, we will incorporate learning by defining the following scattering propagation rule similar to the one used by GCN:

$$\mathbf{X}^\ell = F_{p\text{-scat}}(\mathbf{X}^\ell) = \sigma\left(U_p(\mathbf{X}^{\ell-1} \Theta^\ell)\right). \quad (12)$$

Analogously to GCN, we note the the scattering propagation rule can be decomposed into three steps:

$$\mathbf{X}_{a'}^\ell[w] = \mathbf{X}^{\ell-1}[w] \Theta^\ell \text{ for all } w \in \mathcal{N}_v \quad (13a)$$

$$\mathbf{X}_{b'}^\ell[v] = \left(U_p(\mathbf{X}_{a'}^\ell)\right)[v] \quad (13b)$$

$$\mathbf{X}_{c'}^\ell[v] = \sigma(\mathbf{X}_{b'}^\ell[v])^q. \quad (13c)$$

Importantly, we note that the scattering transform addresses the underreaching problem as wavelets $\Psi_k = \mathbf{P}^{2^{k-1}} - \mathbf{P}^{2^k}$ that are leveraged in the aggregation step (Eq. 13b) have larger receptive fields than most traditional GNNs. However, scattering does not result in oversmoothing because the subtraction results in band-pass filters rather than low-pass filters. In this manner, the scattering transform addresses the challenges discussed in the previous subsection.

4 HYBRID SCATTERING NETWORKS

Here, we introduce two hybrid networks that combine aspects of GCN and the geometric scattering transform discussed in the previous section. Our networks will use both low-pass and band-pass filters in different channels to capture different types of information. As a result, our hybrid networks will have greater expressive power than either traditional GCNs, which only use low-pass filters or a pure scattering network, which only uses band-pass filters.

In our low-pass channels, we use modified GCN filters, which are similar to those used in Eq. 5 but use higher powers of \mathbf{A} and include bias terms. Specifically, we use a channel update rule of the form

$$\mathbf{X}_{\text{low},i}^\ell := \sigma\left(\mathbf{A}^{r_i} \mathbf{X}^{\ell-1} \Theta_{\text{low},i}^\ell + \mathbf{B}_{\text{low},i}^\ell\right) \quad (14)$$

for $1 \leq i \leq C_{\text{low}}$. We note, in particular, that the use of higher powers of \mathbf{A} enables a wider receptive field

3. In a slight deviation from previous work, here U_p does not include the outermost nonlinearity in the cascade.

(of radius r_i), without increasing the number of trainable parameters (unlike in GCN).

Similarly, in our band-pass channels, we use a modified version of Eq. 12, with an added bias term, and our update rule is given by

$$\mathbf{X}_{\text{band},i}^\ell := \sigma\left(U_{p_i}(\mathbf{X}^{\ell-1} \Theta_{\text{band},i}^\ell) + \mathbf{B}_{\text{band},i}^\ell\right) \quad (15)$$

for $1 \leq i \leq C_{\text{band}}$. Here, similarly to Eq. 10, p_i is a path that determines the cascade of wavelets used in the i -th channel.

Aggregation module. Each *hybrid layer* uses a set of C_{low} low-pass and C_{band} band-pass channels to transform the node features $\mathbf{X}^{\ell-1}$, as described in Eq. 14 and Eq. 15, respectively. The resulting filter responses $\{\mathbf{X}_{\text{low},i}^\ell\}_{i=1}^{C_{\text{low}}}$ and $\{\mathbf{X}_{\text{band},i}^\ell\}_{i=1}^{C_{\text{band}}}$ are aggregated to new d_ℓ -dimensional node representations \mathbf{X}^ℓ via an *aggregation module*

$$\mathbf{X}^\ell := \text{AGG}\left(\{\mathbf{X}_{\text{low},i}^\ell\}_{i=1}^{C_{\text{low}}}, \{\mathbf{X}_{\text{band},i}^\ell\}_{i=1}^{C_{\text{band}}}\right). \quad (16)$$

Later, in Sections 4.1 and 4.2, we will discuss two models that use different aggregation modules.

Graph Residual Convolution. After aggregating the outputs of the (low-pass) GCN channels and (band-pass) scattering channels in Eq. 16, we apply the *graph residual convolution*, which acts as a low-pass filtering and aims to eliminate any high-frequency noise introduced by the scattering channels. This noise can arise, for example, if there are various different label rates in different graph substructures. In this case, the scattering features may learn the difference between labeled and unlabeled nodes and thereby produce high-frequency noise.

This filter uses a modified diffusion matrix given by

$$\mathbf{A}_{\text{res}}(\alpha) = \frac{1}{\alpha + 1}(\mathbf{I}_n + \alpha \mathbf{W} \mathbf{D}^{-1}),$$

where the hyperparameter α determines the magnitude of the low-pass filtering. Choosing $\alpha = 0$ yields the identity (no filtering), while $\alpha \rightarrow \infty$ results in the random walk matrix $\mathbf{R} := \mathbf{W} \mathbf{D}^{-1}$. Thus, \mathbf{A}_{res} can be interpreted as lying between a completely lazy random walk that never moves and a non-resting one \mathbf{R} that moves at every time step.

The full residual convolution update rule is given by

$$\mathbf{X}^{\ell+1} := \mathbf{A}_{\text{res}}(\alpha) \mathbf{X}^\ell \Theta_{\text{res}} + \mathbf{B}_{\text{res}}.$$

The multiplication with the weight matrix Θ_{res} corresponds to a fully connected layer applied to the output from Eq. 16 (after low-pass filtering with \mathbf{A}_{res}) with each neuron learning a linear combination of the signals output by the aggregation module.

4.1 Scattering GCN

The Scattering GCN (Sc-GCN) network was first introduced in [33]. Here, the aggregation module concatenates the filter responses horizontally yielding wide node representations \mathbf{X}^ℓ of the form

$$[\mathbf{X}_{\text{low},1}^\ell \parallel \dots \parallel \mathbf{X}_{\text{low},C_{\text{low}}}^\ell \parallel \mathbf{X}_{\text{band},1}^\ell \parallel \dots \parallel \mathbf{X}_{\text{band},C_{\text{band}}}^\ell]. \quad (17)$$

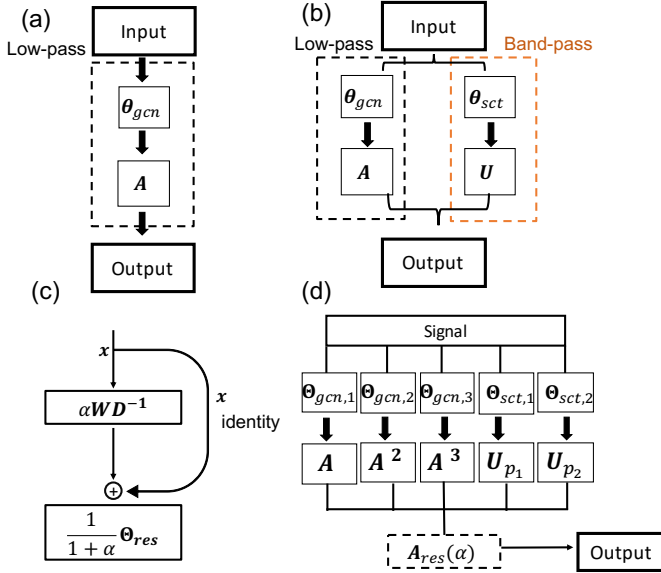


Fig. 2. (a) & (b) comparison between GCN and our Sc-GCN: we add band-pass channels to collect different frequency components; (c) graph residual convolution layer; (d) Sc-GCN combines five network channels, followed by a graph residual convolution.

Sc-GCN then learns relationships between the channels via the graph residual convolution.

Configuration. The primary goal of Sc-GCN is to alleviate oversmoothing in popular semi-supervised node-level tasks on, e.g., citation networks. As regularity patterns in such datasets are often dominated by low-frequency information such as inter-cluster node-similarities, we choose our parameters to focus on low-frequency information. We use three low-pass filters, with receptive fields of sizes radius $r_k = 1, 2, 3$, and two band-pass filters. We use $\sigma(\cdot) := |\cdot|$ as our nonlinearity in all steps except the outermost nonlinearity. Inspired by the aggregation step in classical geometric scattering [13], for the outermost nonlinearity, we additionally apply the q^{th} power at the node level, i.e., $\sigma(\cdot) := |\cdot|^q$.

The paths p and the parameter α from the graph residual convolution are tuned as hyperparameters of the network.

4.2 Geometric Scattering Attention Network

An important observation in Sc-GCN above is that the model decides globally about how to combine different channel information. The network first concatenates all of the features from the low-pass and band-pass channels in Eq. 17 and then combines these features via multiplication with the weight matrix Θ_{res} . However, for complex tasks or datasets, important regularity patterns may vary significantly across different graph regions. In such settings, a model should ideally attend locally over the aggregation and adaptively combine filter responses at different nodes.

This observation inspired the design of the Geometric Scattering Attention Network (GSAN) [34]. Drawing inspiration from [35], GSAN uses an aggregation module based on a multi-head node-level attention framework. However, the attention mechanism used in GSAN differs from [35] by attending over the combination of the different filter

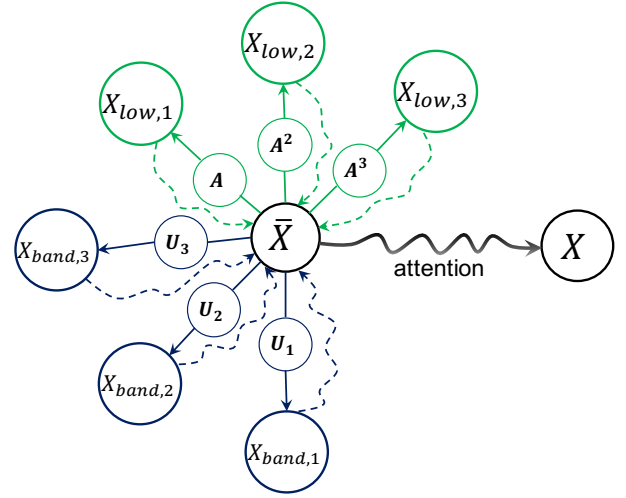


Fig. 3. Illustration of the proposed scattering attention layer.

responses rather than over the combination of node features from neighboring nodes. We will first focus on the processing performed independently by each attention head, and then discuss a multi-head configuration.

In a slight deviation from Sc-GCN, the weight matrices in Eq. 14 and Eq. 15 are shared across the filters of each attention head. Therefore, both aggregation steps (Eq. 6b and Eq. 13b) take the same input denoted by $\bar{X}^\ell := X^{\ell-1} \Theta^\ell$. Next, we define $\bar{X}_{\text{low},i}^\ell := A^{r_i} \bar{X}^\ell$ and $\bar{X}_{\text{band},i}^\ell := |U_{p_i}(\bar{X}^\ell)|$ to be the outputs of the aggregation steps, Eq. 6b and Eq. 13b, with the bias terms set to zero. We then compute *attention score vectors* $e_{\text{low},i}^\ell, e_{\text{band},i}^\ell \in \mathbb{R}^n$ that will be used to determine the importance of each of the filter responses for every single node. We calculate

$$e_{\text{low},i}^\ell = \text{LeakyReLU} \left(\left[\bar{X}^\ell \parallel \bar{X}_{\text{low},i}^\ell \right] \mathbf{a} \right),$$

with analogous $e_{\text{band},i}^\ell$ and $\mathbf{a} \in \mathbb{R}^{2d_\ell}$ being a learned *attention vector* that is shared across all filters of the attention head. These attention scores are then normalized across all filters using the softmax function. Specifically, we define

$$\alpha_{\text{low},j}^\ell := \frac{\exp(e_{\text{low},j}^\ell)}{\sum_{i=1}^{C_{\text{low}}} \exp(e_{\text{low},i}^\ell) + \sum_{i=1}^{C_{\text{band}}} \exp(e_{\text{band},i}^\ell)},$$

where the exponential function is applied elementwise, and define $\alpha_{\text{band},j}^\ell$ analogously. Finally, for every node, the filter responses are summed together, weighted by the corresponding (node-to-filter) attention score. We also normalize by the number of filters $C := C_{\text{low}} + C_{\text{band}}$, which gives

$$X^\ell = C^{-1} \tilde{\sigma} \left(\sum_{j=1}^{C_{\text{low}}} \alpha_{\text{low},j}^\ell \odot \bar{X}_{\text{low},j}^\ell + \sum_{j=1}^{C_{\text{band}}} \alpha_{\text{band},j}^\ell \odot \bar{X}_{\text{band},j}^\ell \right),$$

where $\alpha \odot X := \text{diag}(\alpha) X$ denotes the Hadamard (elementwise) product of α with each column of X . We further use $\tilde{\sigma}(\cdot) = \text{ReLU}(\cdot)$ in the equation above.

Multi-head Attention. Similar to other applications of attention mechanisms [35], we use multi-head attention to stabi-

lize the training, thus yielding as output of the aggregation module (by a slight abuse of notation)

$$\mathbf{X}^\ell = \|\Gamma_{\gamma=1} \mathbf{X}_\gamma^\ell (\Theta_\gamma^\ell, \alpha_\gamma^\ell), \quad (18)$$

concatenating Γ attention heads. As explained above, each attention head has individual trained parameters Θ_γ^ℓ and α_γ^ℓ and outputs a filter response \mathbf{X}_γ^ℓ . Similar to Sc-GCN, this concatenation results in wide node representations that are further refined by the graph residual convolution.

Configuration. For GSAN, we set $C_{\text{low}} = C_{\text{band}} = 3$, giving the model balanced access to both low-pass and band-pass information. The aggregation process of the attention layer is shown in Fig. 3, where $U_{1,2,3}$ represent three first-order scattering transformations with $U_1 \mathbf{x} := \Psi_1 \mathbf{x}$, $U_2 \mathbf{x} := \Psi_2 \mathbf{x}$ and $U_3 \mathbf{x} := \Psi_3 \mathbf{x}$. The number of attention heads Γ and the parameter α from the graph residual convolution are tuned as hyperparameters of the network.

5 THEORY OF HYBRID SCATTERING NETWORKS

In this section, we analyze the ability of scattering filters to capture information not captured by traditional GCN filters. As discussed in Section 3.3, GCN filters effectively act as localized averaging operators and focus primarily on low-frequency information. By contrast, band-pass filters are able to retain high-frequency information and a broader class of regularity patterns. As a simple example, we recall Lemma 1 of [33]. This result considers a two-periodic signal on a cycle graph with an even number of nodes. It shows that Eq. 3 yields a constant signal as filter response, while the scattering filter $\Psi_0 \mathbf{x}$ from Eq. 9 still produces a two-coloring signal. Inductively, we note that this result may be extended to any finite linear cascade of such filters, i.e., $\mathbf{g}_{\theta_k} * \dots * \mathbf{g}_{\theta_1} * \mathbf{x}$ or $\Psi_0 \dots \Psi_0 \mathbf{x}$. Moreover, Lemma 2 of the same paper shows that this result may be generalized considerably and can be extended to any two-coloring of a regular bipartite graph.

In the context of semi-supervised learning, these results imply that on a bipartite graph, a GCN-based method cannot be used to predict which part of the vertex set a given node belongs to (assuming that the input feature is a two-coloring of the graph). However scattering methods preserve two-colorings and therefore will likely be successful for this task. Here, we will further develop this theory and analyze the advantages of our hybrid scattering networks on more general graphs.

Our analysis will be based on a notion of *node discriminability*⁴, which intuitively corresponds to a network producing different representations of two nodes v and w in its hidden layers. We will let \mathcal{N}_v^K denote the K -step node neighborhood⁴ of a node v (including v itself), and for $V_S \subset V$ we will let $G(V_S)$ denote the corresponding *induced subgraph*⁴. We will say two induced subgraphs $G(V_S)$ and $G(V_{S'})$ are *isomorphic*⁴ if they have identical geometric structure and write $G(V_S) \cong^\phi G(V_{S'})$ to indicate that ϕ is an isometry (geometry preserving map) between them. In the definition below, we introduce a class of *graph-intrinsic* node features that encode graph topology information. We

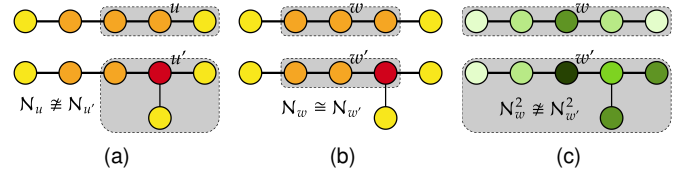


Fig. 4. Intrinsic node features for two graphs (top/bottom). We compare nodes from the isomorphic horizontal path that is part of both graphs. Color coding indicates different node feature values and differs in (c). Node features are one-intrinsic (degrees) in (a) and (b), and two-intrinsic (average degree in one-step neighborhoods) in (c). Gray area represents subgraph used for the feature assignment at the indicated node.

will use these features as the input for GNN models in order to produce geometrically informed node representations.

Definition 1 (Intrinsic Node Features). A nonzero node feature matrix \mathbf{X} is K -intrinsic if for any $v, w \in V$ such that $G(\mathcal{N}_v^K)$ is isomorphic to $G(\mathcal{N}_w^K)$, we have $\mathbf{X}[v] = \mathbf{X}[w]$.

These intrinsic node features encode important K -local geometric information in the sense that if $\mathbf{X}[v] \neq \mathbf{X}[w]$, then the K -step neighborhoods of v and w must have different geometric structure. To further understand this definition, we observe that the degree vector, or any (elementwise) function of it, is a one-intrinsic node feature matrix. Setting $\mathbf{X}[v]$ to the average node degree of nodes in \mathcal{N}_v^{K-1} yields K -intrinsic node features. As a slightly more complicated example, features with $\mathbf{X}[v]$ the number of triangles contained in \mathcal{N}_v^K are also K -intrinsic. Fig. 4 illustrates how such node features can help distinguish nodes from different graph structures.

As a concrete example, consider the task of predicting traffic on a network of Wikipedia articles, such as the Chameleon dataset [36], with nodes and edges corresponding to articles and hyperlinks. Here, intrinsic node features provide insights into the topological context of each node. A high degree suggests a widely cited article, which is likely to have a lot of traffic, while counting k -cliques or considering average degrees from nearby nodes can shed light on the density of the local graph region.

The following theorem characterizes situations when GCN filters cannot discriminate nodes based on the information represented in intrinsic node features.

Theorem 1. Let $\phi : V \rightarrow V$, $v \in V$, and $K, L \in \mathbb{N}$ such that $G(\mathcal{N}_v^{K+L}) \cong^\phi G(\mathcal{N}_{\phi(v)}^{K+L})$. Let \mathbf{X}^0 be any K -intrinsic node feature matrix and let \mathbf{X}^ℓ be the output of an ℓ -layer GCN, i.e., $F_{\text{gc}}^\ell \circ \dots \circ F_{\text{gc}}^1$, with each layer as in Eq. 5. Then, for any $0 \leq \ell \leq L$, we have $\mathbf{X}^\ell[v] = \mathbf{X}^\ell[\phi(v)]$. Therefore, the nodes v and $\phi(v)$ cannot be discriminated based on the filtered node features \mathbf{X}^ℓ from an ℓ -layer GCN.

Below, we provide a sketch of the main ideas of the proof. For a complete proof, please see Appendix A.2.

Proof Sketch. We use induction to show $\mathbf{X}^\ell[u] = \mathbf{X}^\ell[\phi(u)]$ for all $u \in \mathcal{N}_v^{L-\ell}$ and all $0 \leq \ell \leq L$. The case $\ell = 0$ follows from Definition 1. One may then establish the inductive step by showing that the steps Eq. 6a-6c preserve this equality for all $u \in \mathcal{N}_v^{L-(\ell+1)}$. Therefore, $\mathbf{X}[u]^\ell = \mathbf{X}^\ell[\phi(u)]$ for all $0 \leq$

4. Formal definitions are provided in Appendix. A.1,

$\ell \leq L$ and so an ℓ -layer GCN cannot be used to distinguish these nodes. \square

Next, we introduce a notion of structural difference that allows us to analyze situations where scattering networks have strictly greater discriminatory power than GCNs.

Definition 2 (Structural Difference). For two ϕ -isomorphic induced subgraphs $G(V_S) \cong^\phi G(V_{S'})$, a *structural difference* relative to ϕ and a node feature matrix \mathbf{X} is manifested at $u \in V_S$ if $\mathbf{X}[u] \neq \mathbf{X}[\phi(u)]$ or $d_u \neq d_{\phi(u)}$.⁵

Notably, if the K -step neighborhoods of two nodes are ϕ -isomorphic and \mathbf{X} is any K -intrinsic node feature matrix, then no structural difference relative to ϕ and \mathbf{X} can be manifested at u . Theorem 2 stated below shows that a scattering network will be able to produce different representations of two nodes v and $\phi(v)$ if there are structural differences in their surrounding neighborhoods, assuming (among a few other mild assumptions) that a certain pathological case is avoided. The next definition characterizes this pathological situation that arises, roughly speaking, when two sums $\sum_i a_i$ and $\sum_i b_i$ coincide, even though $a_i \neq b_i$ for all i . We note that although this condition seems complicated, it is highly unlikely to occur in practice.

Definition 3 (Coincidental Correspondence). Let $\phi : V \rightarrow V$ and $u \in V$ such that $G(\mathcal{N}_u) \cong^\phi G(\mathcal{N}_{\phi(u)})$. Let \mathbf{X} be a node feature matrix, and let

$$\Delta_u := \{w \in \mathcal{N}_u : \text{struc. difference rel. to } \phi \text{ and } \mathbf{X} \text{ at } w\}.$$

We say that a node u is subject to *coincidental correspondence* relative to ϕ and \mathbf{X} if Δ_u is non-empty and

$$\sum_{w \in \Delta_u} d_w^{-1} \mathbf{X}[w] = \sum_{w \in \phi(\Delta_u)} d_w^{-1} \mathbf{X}[w]. \quad (19)$$

We further say that a set of nodes $U \subset V$ is subject to *coincidental correspondence* if there exists at least one $u \in U$ that is subject to coincidental correspondence.

Remark 1. When assuming there is *no* coincidental correspondence relative to ϕ and \mathbf{X} on a set of nodes $U = \text{int}(\mathcal{N}_v^d)$ for some $d \in \mathbb{N}$, we will implicitly assume this to also hold for diffused node features obtained from multiple diffusions via \mathbf{P} or cascades of wavelets and nonlinear activations σ with *spatial support*⁴ up to a radius of $d - 1$.

Theorem 2. *As in Theorem 1, let $\phi : V \rightarrow V$, $v \in V$, and $K, L \in \mathbb{N}$ such that $G(\mathcal{N}_v^{K+L}) \cong^\phi G(\mathcal{N}_{\phi(v)}^{K+L})$, and consider any K -intrinsic node feature matrix \mathbf{X} . Further assume that there exists at least one structural difference rel. to ϕ and \mathbf{X} in \mathcal{N}_v^{K+L} , and let $1 \leq d \leq K + L$ be the smallest positive integer such that a structural difference is manifested in \mathcal{N}_v^d . If the nonlinearity σ is strictly monotonic and $\text{int}(\mathcal{N}_v^d)$ is not subject to coincidental correspondence rel. to ϕ and \mathbf{X} , then one can define a scattering configuration (p, Θ) such that scattering features $F_{p\text{-scat}}(\mathbf{X})$ defined as in Eq. 12 discriminate v and $\phi(v)$.*

Theorem 2 provides a large class of situations where scattering filters are able to discriminate between two nodes

⁵ Note that $d_u \neq d_{\phi(u)}$ is only relevant for nodes in the *boundary*⁴ ∂S because $d_w = d_{\phi(w)}$ for all *interior*⁴ nodes $w \in \text{int}(S)$, as the degree is 1-intrinsic. For $u \in \partial S$, we further assume $d_{\phi(u)} \mathbf{X}[u] \neq d_u \mathbf{X}[\phi(u)]$.

even if GCN filters are not. In particular, even if the $K + L$ step neighborhood of v and $\phi(v)$ are isomorphic, it is possible for there to exist a u in this $K + L$ step neighborhood such that a K -intrinsic node feature takes different values at u and $\phi(u)$. Theorem 2 shows that scattering will produce differing representations of these two nodes (i.e., v and $\phi(v)$), while Theorem 1 shows that GCN will not. The following two remarks discuss minor variations of Theorem 2.

Remark 2. The absolute value operation is not monotonic. Therefore, Theorem 2 cannot be directly applied in this case. However, the above result and all subsequent results can be extended to the case $\sigma = |\cdot|$ as long as certain pathological cases are avoided. Namely, Theorem 2 will remain valid as long as the features at u are assumed not to be negatives of the features at $\phi(u)$, i.e., $\mathbf{X}[u] \neq -\mathbf{X}[\phi(u)]$ for nodes $u \in \text{int}(\mathcal{N}_v^d)$, and similarly to Remark 1, we also must assume that the diffused node features are not negatives of each other. We note that while this condition is complex, it is rarely violated in practice.

Remark 3. A result analogous to Theorem 2 is also valid for any permutation of the three steps Eq. 13a-13c (even with added bias terms as in Eq. 15). In particular, it applies to the update rule

$$\mathbf{X}^\ell = \sigma \left(\mathbf{U}_p (\mathbf{X}^{\ell-1}) \Theta^\ell + \mathbf{B}^\ell \right).$$

We will provide a full sketch of the proof of Theorem 2 here and provide details in the appendix. The key to the proof will be applying Lemma 1 stated below. In order to explain these ideas, we must first introduce some notation that partition the neighborhoods \mathcal{N}_v^{K+L} from Theorem 2 into a set of node layers that are parameterized by their minimal distance from v .

Notation 1. Let $\phi : V \rightarrow V$, $v \in V$, $D \in \mathbb{N}$, such that $G(\mathcal{N}_v^D) \cong^\phi G(\mathcal{N}_{\phi(v)}^D)$. Assume that there exists at least one node in \mathcal{N}_v^D , where a structural difference is manifested rel. to ϕ and node features \mathbf{X} . We define

$$V_{\text{diff}} := \left\{ u \in \mathcal{N}_v^D : \text{struc. difference rel. to } \phi \text{ and } \mathbf{X} \text{ at } u \right\}.$$

and we fix the following notations:

- (i) Let $d := \min\{d(u, v) : u \in V_{\text{diff}}\}$ and define the node set $V_{\text{diff}}^d := \{u \in V_{\text{diff}} : d(u, v) = d\}$. Note that these are exactly the nodes in \mathcal{N}_v^d where a structural difference is manifested relative to ϕ and \mathbf{X} .
- (ii) Let $\tau \in \mathbb{N}$ be the number of paths of minimal length between v and vertices in V_{diff}^d , and denote these by $p^{(i)} := (u_0^i, \dots, u_d^i = v)$ with $u_0^i \in V_{\text{diff}}^d$ for $1 \leq i \leq \tau$.
- (iii) Let $U_j := \cup_{i=1}^\tau \{u_j^{(i)}\}$, and define the *generalized path* from V_{diff}^d to v as $P := (U_0, U_1, \dots, U_d)$.

With this notation established, we may now state the following lemma which is critical to the proof of Theorem 2.

Lemma 1. *Let $\phi : V \rightarrow V$, $\tilde{v} \in V$, and $\tilde{D} \in \mathbb{N}$ such that $G(\mathcal{N}_{\tilde{v}}^{\tilde{D}}) \cong^\phi G(\mathcal{N}_{\phi(\tilde{v})}^{\tilde{D}})$. Assume there exists at least one node in $\mathcal{N}_{\tilde{v}}^{\tilde{D}}$ where a structural difference is manifested relative to ϕ and to $\tilde{\mathbf{X}}$, and let $1 \leq \tilde{d} \leq \tilde{D}$ be the smallest positive integer*

such that a structural difference is manifested in $\mathcal{N}_{\tilde{v}}^{\tilde{d}}$. Assume that $\text{int}\left(\mathcal{N}_{\tilde{v}}^{\tilde{d}}\right)$ is not subject to coincidental correspondence relative to ϕ and $\tilde{\mathbf{X}}$, and let $\tilde{P} := (\tilde{U}_0, \tilde{U}_1, \dots, \tilde{U}_{\tilde{d}})$ be the generalized path as defined in Notation 1. Then, for $j = 0, \dots, \tilde{d}$, the nodes in \tilde{U}_j are exactly the nodes in $\mathcal{N}_{\tilde{v}}^{\tilde{d}-j}$ where a structural difference is manifested relative to ϕ and filtered node features $\mathbf{Y}^j := \mathbf{P}^j \tilde{\mathbf{X}}$.

Below, we provide a sketch of the main ideas of the proof. A complete proof is provided in Appendix A.3.

Proof Sketch. The main idea of the proof is to use induction to show that at every step the matrix \mathbf{P} propagates the information about the structural difference one node layer closer towards \tilde{v} .

By Notation 1(i), we have $\tilde{U}_0 = V_{\text{diff}}^{\tilde{d}}$. Therefore, the case $j = 0$ is immediate. In the inductive step, it suffices to show

$$\mathbf{Y}^{j+1}[u] \neq \mathbf{Y}^{j+1}[\phi(u)]$$

for all $u \in \tilde{U}_{j+1}$ and

$$\mathbf{Y}^{j+1}[w] = \mathbf{Y}^{j+1}[\phi(w)]$$

for all $w \in \mathcal{N}_{\tilde{v}}^{\tilde{d}-(j+1)} \setminus \tilde{U}_{j+1}$ under the assumption that these results are already valid for \mathbf{Y}^j . This can be established by writing $\mathbf{P}^{j+1} \tilde{\mathbf{X}} = \mathbf{P} \mathbf{P}^j \tilde{\mathbf{X}} = \mathbf{P} \mathbf{Y}^j$ and using the inductive hypothesis together with the definition of \mathbf{P} . \square

We now use Lemma 1 to sketch the proof of Theorem 2. The complete proof is provided in Appendix A.4.

Proof Sketch for Theorem 2. We need to show that we can choose the parameters in a way that guarantees $F_{p\text{-sct}}(\mathbf{X})[v] \neq F_{p\text{-sct}}(\mathbf{X})[\phi(v)]$. For simplicity, we set $\Theta = \mathbf{I}_n$. In this case, since σ strictly monotonic, and therefore injective, it suffices to show that we can construct p such that

$$U_p(\mathbf{X})[v] \neq U_p(\mathbf{X})[\phi(v)]. \quad (20)$$

Using binary expansion, we may choose $k_1, \dots, k_m \in \mathbb{N}_0$, $k_i < k_{i+1}$, such that $d = 2^{k_1} + \dots + 2^{k_m}$ and set $p := (k_1, \dots, k_m)$. Given p , we define truncated paths $p_{:i} := (k_1, \dots, k_i)$ and let $t_i := \sum_{j=1}^i 2^{k_j}$ for $1 \leq i \leq m$. For $i = 0$, we let $p_{:0}$ denote the empty path of length 0 and set $t_0 = 0$.

Recalling the generalized path $P = (U_0, \dots, U_d)$ defined in Notation 1, we will use induction to show that U_{t_i} is equal to the set of nodes in $\mathcal{N}_{\tilde{v}}^{d-t_i}$ such that a structural difference is manifested relative to ϕ and $\mathbf{Z}^i := U_{p_{:i}} \mathbf{X}$ for $0 \leq i \leq m$. Since $t_m = d$ and $p_{:m} = p$, this will imply Eq. 20 and thus prove the theorem. Analogously to the base case in the proof of Lemma 1, the case $i = 0$ follows from Notation 1(i). In the inductive step, it suffices to show that

$$\mathbf{Z}^{i+1}[u] \neq \mathbf{Z}^{i+1}[\phi(u)],$$

for all $u \in U_{t_{i+1}}$ and

$$\mathbf{Z}^{i+1}[w] = \mathbf{Z}^{i+1}[\phi(w)],$$

for all $w \in \mathcal{N}_{\tilde{v}}^{d-t_{i+1}} \setminus U_{t_{i+1}}$, under the assumption that these results are true for i . Since $\mathbf{Z}^{i+1} = \Psi_{k_{i+1}}(\mathbf{Z}^i)$ and σ is increasing and therefore injective, it suffices to show that these results are preserved under multiplication by a

wavelet matrix $\Psi_{k_{i+1}} = \mathbf{P}^{2^{k_{i+1}-1}} - \mathbf{P}^{2^{k_{i+1}}}$. This can be verified using Lemma 1 (with $\sigma(\mathbf{Z}^i)$ in place of $\tilde{\mathbf{X}}$) and the inductive hypothesis. \square

Remark 4. In the proof of Theorem 2, for the sake of concreteness, we chose $\Theta = \mathbf{I}_n$ and p such that $|p| = \sum_{j=1}^m 2^{k_j} = d$. However, inspecting the proof we see that we may choose p to be any path with $|p| \geq d$ and also that the choice of Θ does not matter as long as Θ is invertible. In particular, if the entries of Θ are generated i.i.d. at random from a continuous probability distribution, the conclusions of the theorem will hold with probability one (see e.g. [37]). We also note that both Theorems 1 and 2 may be extended to the case where the update rule features a bias term \mathbf{B} as in Eq. 14 and 15 since the mapping $\mathbf{X} \rightarrow \mathbf{X} + \mathbf{B}$ is injective.

In Appendix A.5, we will also present a modified version of Theorem 2, where the assumption on coincidental correspondence is replaced by an assumption on the (generalized) path between the structural differences and the investigated node.

6 EMPIRICAL RESULTS

We now present our empirical results starting with semi-supervised node classification. We first show that our hybrid Sc-GCN model [33] is able to overcome the oversmoothing problem and in particular exhibits superior performance to either a pure GCN Network or a pure scattering network on node-classification tasks. We then show that we can further improve performance, particularly on complex datasets, by using GSAN [34], which incorporates an attention mechanism. After that, we turn to graph-level tasks and establish that our hybrid scattering models also perform very well in such settings.

6.1 Semi-Supervised Node Classification

Scattering GCN. We compare the performance of Sc-GCN to both the original GCN [5] as well as the closely related Cheb-Net [28] and a network which uses Gaussian random fields to propagate label information [38]. Additionally, we compare against [14], which uses a pure-scattering approach. Further, we also compare Sc-GCN to two methods designed, in part, to address the oversmoothing problem. In [9], this problem is directly addressed by using partially absorbing random walks [39] to slow the mixing of node features in regions of the graph with high connectivity. The GAT graph attention network from [10], on the other hand, addresses this problem indirectly by using an attention mechanism to train an adaptive node-wise weighting of the smoothing operation. Lastly, as a baseline we used an SVM classifier that acts directly on the node features while ignoring the graph structure.

In our experiments, we used four popular datasets summarized in Tab. 1. For full details on these datasets, please see, e.g., [40] for Citeseer, Cora, and Pubmed and [41] for DBLP. As discussed in [9], the oversmoothing problem is most acute in highly connected networks where information mixes rapidly and nodes quickly become indistinguishable. Therefore, we included networks with different size and connectivity structures and order the datasets by connectivity structure (with the most connected on the right).

TABLE 1

Dataset characteristics: number of nodes, edges, and features; mean \pm std. of node degrees; ratio of #edges to #nodes.

Dataset	Nodes	Edges	Features	Degrees	$\frac{\text{Edges}}{\text{Nodes}}$
Citeseer	3,327	4,732	3,703	3.77 ± 3.38	1.42
Cora	2,708	5,429	1,433	4.90 ± 5.22	2.00
Pubmed	19,717	44,338	500	5.50 ± 7.43	2.25
DBLP	17,716	52,867	1639	6.97 ± 9.35	2.98

TABLE 2

Classification accuracy (top two marked in bold; best one underlined) of Scattering GCN on four benchmark datasets (ordered by increasing connectivity) compared to four other GNNs [5], [9], [10], [28], a non-GNN approach [38] based on belief propagation, a pure graph scattering baseline [14], and a nongeometric baseline only using node features with linear SVM.

Model	Citeseer	Cora	Pubmed	DBLP
Sc-GCN (ours)	71.7	84.2	79.4	81.5
GAT [10]	<u>72.5</u>	83.0	79.0	66.1
Partially absorbing [9]	71.2	81.7	79.2	56.9
GCN [5]	70.3	81.5	79.0	59.3
Chebyshev [28]	69.8	78.1	74.4	57.3
Label Propagation [38]	58.2	77.3	71.0	53.0
Graph scattering [14]	67.5	81.9	69.8	69.4
Node features (SVM)	61.1	58.0	49.9	48.2

Consistent with our expectation, Tab. 2 and Fig. 5 show that the advantages of our network are most significant for the networks with high-connectivity.

We implemented all of these methods based upon the code made available by the original authors, and, for fair comparison, we tuned and evaluated each of these methods using the standard splits provided for benchmark datasets. Whenever possible, we made sure that our results are consistent with previously reported accuracies. We tuned our method, both the hyperparameters and number of scattering and GCN channels, via a grid search (over the same set for all datasets), and we used the same cross-validation procedure for our method and the competing methods. In appendix (Sec. B), we provide further details and also perform an ablation study evaluating the importance of each component in our proposed architecture.

We report test classification accuracy in Tab. 2, which shows that our approach outperforms other methods on three out of the four considered datasets. Only on Citeseer, we are slightly outperformed by GAT. However, this is the dataset with the weakest connectivity structure (see Tab. 1), while at the same time having the most informative node features (achieving 61.1% accuracy via linear SVM without considering graph information). In contrast, on DBLP, which exhibits the richest connectivity structure and least informative features (only 48.2% SVM accuracy), we significantly outperform GAT (by over 15% improvement). Notably, GAT itself significantly outperforms all other methods (by 6.8% or more) apart from the graph scattering baseline [14].

The task of semi-supervised learning is motivated by the fact that in real-world applications one typically only has labels for a small fraction of the nodes. Therefore, we next analyze the performance of our network with limited amounts of training data. Fig. 5 (top) plots the training accuracy of Sc-GCN, as well as the other networks (except the baselines), as the amount of training data varies from

20% to 100% of its original amount. Across all networks, we see that Sc-GCN exhibits the best performance when the training data is sufficiently limited. Moreover, we see that it outperforms GAT, which is the next best performing network in terms of overall accuracy (see Tab. 2), on all datasets whenever the training data is reduced to 60% of its original size or less.

In Fig. 5 (bottom), we plot the evolution of the validation error during the training process. We note that Sc-GCN is able to reach a low training error significantly faster than GAT, which is the next most competitive in terms of overall accuracy. Several other methods do achieve low validation errors faster on several datasets, but their final accuracy is much lower than that of Sc-GCN. Moreover, on Pubmed, which is the largest dataset, Sc-GCN achieves a low validation error at about the same rate as GCN and at a significantly faster rate than all other methods.

Geometric Scattering Attention Network. Having established the practical utility of the hybrid network Sc-GCN above, we next show that performance may be further improved by using GSN, which builds upon Sc-GCN by incorporating an attention mechanism. We evaluate performance again for semi-supervised node classification, and compare to two popular models (namely GCN [5] and GAT [10]), as well as the original Sc-GCN. We extend our experiments to eight benchmark datasets that we order according to increasing homophily, as shown in Tab. 3. The homophily of a graph is quantified by the fraction of edges that connect nodes that share the same label. High homophily indicates a relatively smooth label distribution, while low homophily suggests a more complex labeling pattern. Texas and Chameleon are low-homophily datasets where nodes correspond to webpages and edges to links between them, with classes corresponding to webpage topic or monthly traffic (discretized into five levels), respectively [42]. Wiki-CS consists of nodes that represent computer science articles with the edges representing the hyperlinks [43]. CoraFull is the larger version of the Cora dataset [44]. The remaining four datasets (i.e., Cora, Citeseer, Pubmed, DBLP) are the citation networks that we already studied when evaluating Sc-GCN above. Notably, compared to the added datasets, the latter four exhibit relatively high homophily.

We split the datasets into train, validation and testing sets. The hyperparameters (number of attention heads Γ , residual parameter α and channel widths) are tuned via grid search using the validation set.

The results in Tab. 3 show that both Sc-GCN and GSN outperform GCN and GAT on seven out of eight datasets. The advantages of GSN over Sc-GCN are particularly notable on the medium-size and large datasets Chameleon and CoraFull that exhibit relatively low-homophily. The most striking result is for Chameleon. Here, Sc-GCN clearly outperforms GCN and GAT (by at least 8.2%), but GSN considerably improves performance even more (by additional 10%).

Analyzing the node-wise attention weights (see Sec. 4.2) allows us to understand the importance of different channels for different datasets. We consider here the ratio between attention assigned to band-pass and low-pass channels (over all attention heads). For that, we first sum up at-

TABLE 3

Dataset characteristics & comparison of node classification test accuracy. Datasets are ordered by increasing homophily.

Dataset	Classes	Nodes	Edges	Homophily	GCN	GAT	Sc-GCN	GSAN
Texas	5	183	295	0.11	59.5	58.4	60.3	60.5
Chameleon	5	2,277	31,421	0.23	28.2	42.9	51.2	61.2
CoraFull	70	19,793	63,421	0.57	62.2	51.9	62.5	64.5
Wiki-CS	10	11,701	216,123	0.65	77.2	77.7	78.1	78.6
Citeseer	6	3,327	4,676	0.74	70.3	72.5	71.7	71.3
Pubmed	3	19,717	44,327	0.80	79.0	79.0	79.4	79.8
Cora	7	2,708	5,276	0.81	81.5	83.0	84.2	84.0
DBLP	4	17,716	52,867	0.83	59.3	66.1	81.5	84.3

tention over low-pass and band-pass channels, respectively, i.e., $\alpha_{\text{low}} := \sum_{\gamma} \sum_i \alpha_{\text{low},i}^{\gamma}$ and $\alpha_{\text{band}} := \sum_{\gamma} \sum_i \alpha_{\text{band},i}^{\gamma}$. Then, for each node v , we calculate the ratio $\zeta_v := \alpha_{\text{band}}[v] / \alpha_{\text{low}}[v]$. In Fig. 6, we present the distributions of $\{\zeta_v : v \in V\}$ for four datasets.

Examining the distributions, we observe four different dataset profiles. Citeseer and WikiCS exhibit minimal spread of attention ratios. In Citeseer, most of the attention is given to the low-pass channels, while WikiCS shows very balanced channel usage. In contrast, DBLP and Chameleon exhibit large spreads. Although the majority of nodes in both datasets values low-pass filters more, some nodes in Wiki-CS pay up to five times the attention to band-pass channels compared to low-pass ones (and vice versa). Interestingly, the distribution for Chameleon has two peaks, suggesting two node populations that require different band-information, which we interpret to be a driving factor for the improvement of GSAN on Chameleon (see Tab. 3).

6.2 Graph Classification and Regression

Graph Classification. We use COLLAB and IMBD-BINARY as benchmark datasets. These are ego networks extracted

from scientific collaborations and movie collaborations, respectively [45]. COLLAB contains 5,000 graphs with three classes and IMBD-BINARY contains 1,000 graphs with two classes. We use a 80-10-10 split between training, validation and test. The datasets contain graph structures but no associated graph signals. In our work, we compute the eccentricity (for connected graphs), degree and clustering coefficient of each vertex, and use these as input signals to our network.

We use one-layer GSAN with 8 heads and 16 hidden units for COLLAB and one-layer GSAN with 4 heads and 16 hidden units for IMBD-BINARY, followed by one graph residual convolutional layer. We then apply a Set2Set module [46] followed by a multi-layer perceptron (MLP). Set2Set is a graph pooling architecture [47] where we apply an LSTM-based module for k processing steps iteratively on the graph signal. During each processing step, node-wise feature signals with variable graph size are integrated using a LSTM-based attention mechanism. In our model, the GSAN-based layer outputs a graph signal $\mathbf{X} \in \mathbb{R}^{n \times d}$ and the Set2Set layer outputs a graph level feature vector $\text{Set2Set}(\mathbf{X}) \in \mathbb{R}^{2d}$ for each graph. After the Set2Set layer, we apply an MLP layer $\mathbb{R}^{2d} \rightarrow \mathbb{R}$ on the graph level signal for the classification task. We use a Set2Set layer with 3

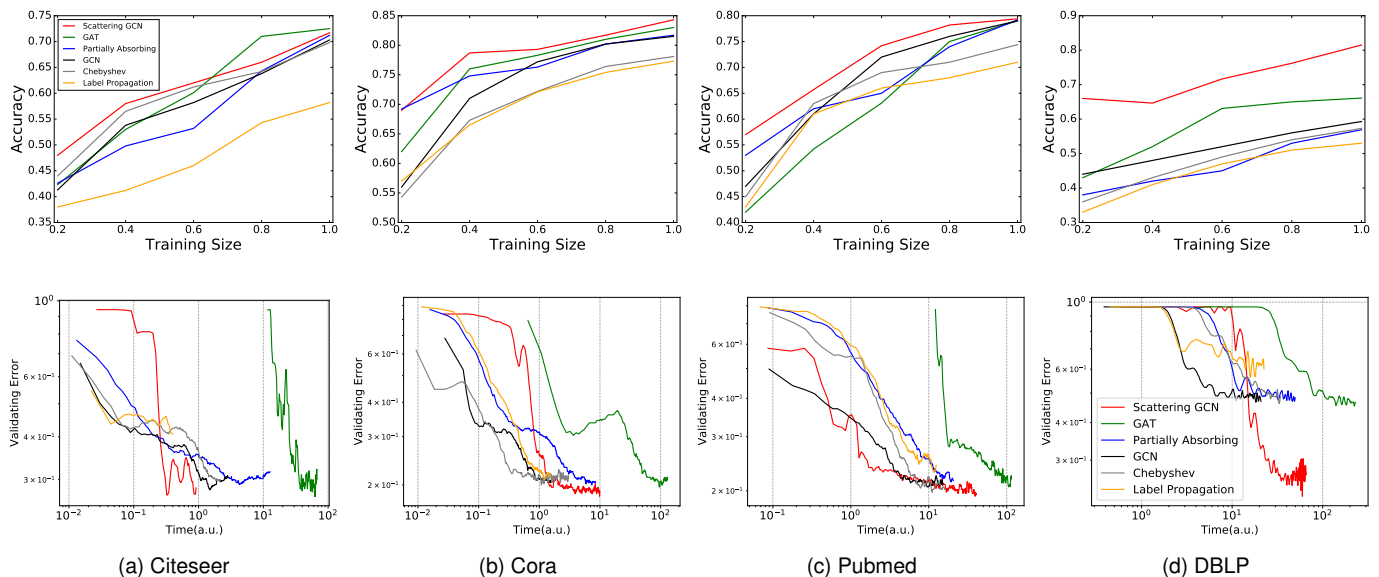


Fig. 5. Impact of training set size (top) and training time (bottom) on classification accuracy and error (correspondingly); training size measured relative to the original training size of each dataset; training time and validation error plotted in logarithmic scale; runtime measured for all methods on the same hardware, using original implementations accompanying their publications.

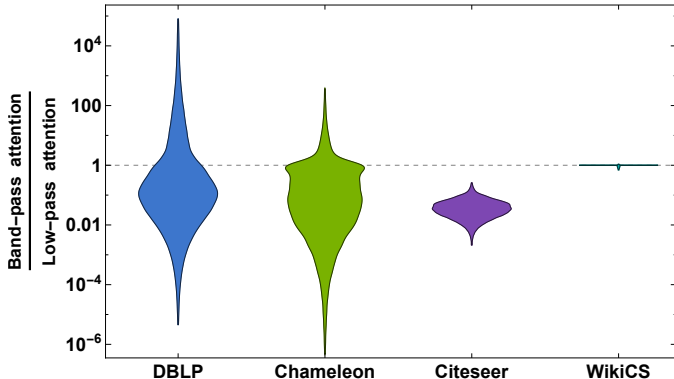


Fig. 6. Distribution of attention ratios per node between band-pass (scattering) and low-pass (GCN) channels across all heads for DBLP, Chameleon, Citeseer, and WikiCS.

processing steps and a two-layer MLP for graph pooling. Our results in Tab. 4 show that both proposed hybrid scattering networks show improvement over the compared baselines.

TABLE 4

Comparison of graph classification test accuracy (higher is better).

Dataset	GCN	GAT	GS-SVM	Sc-GCN	GSAN
COLLAB	0.592	0.523	0.640	0.690	0.704
IMBD-BINARY	0.710	0.632	0.710	0.740	0.760

Graph Regression. We use ZINC and Lipophilicity as benchmark datasets [48], [49]. For the ZINC dataset, the target is the penalized water-octanol partition coefficient of different molecules. For the Lipophilicity dataset, the task is predicting the experimental octanol/water distribution coefficient of different molecules. ZINC contains 1,000 graphs and Lipophilicity contains 4,200 graphs. Graphs in ZINC have 75 input features and graphs in Lipophilicity have 9 input features. We use a 80-10-10 split between training, validation and testing.

We again use a GSAN-based approach, this time consisting of two geometric scattering attention layers followed by one graph residual convolution layer. For ZINC, we use a 32-head GSAN with 32 hidden units as the first scattering layer and an one-head GSAN with 128 hidden units as the second layer. For Lipophilicity, we use a 4-head GSAN with 32 hidden units as the first scattering layer and an one-head GSAN with 96 hidden units as the second layer. The aggregation module uses an MLP, applied to the output node representations, producing a scalar output, followed by an average pooling on each molecule. Our results are presented in Tab. 5, demonstrating the utility of our GSAN approach for this task as well.

TABLE 5

Comparison of graph regression test error (lower is better).

Dataset	GCN	GAT	Sc-GCN	GSAN
ZINC	0.469	0.463	0.452	0.430
Lipophilicity	1.05	0.950	1.03	1.02

7 CONCLUSION

Here, we studied GNN approaches for semi-supervised node classification and investigate some of the major limitations of today’s architectures. Many popular models are known to essentially rely on the low-pass filtering of graph signals. Based on this observation, we propose a novel hybrid GNN framework that can leverage higher frequency information not captured by traditional GCN models. Our construction is based on geometric scattering, a concept that was previously used mainly for graph classification, which we adapt to the node level. We demonstrated theoretically that the resulting scattering filters are more sensitive to the graph topology than traditional GCN when used in conjunction with node features that encode graph structure information. Empirically, we first evaluated our Sc-GCN model and demonstrated its efficacy in alleviating so-called oversmoothing. We then evaluated our GSAN model, which further improves performance, particularly in more complex (low-homophily) settings, via an attention framework. We also provide evidence that the proposed hybrid scattering networks perform well in graph-level tasks, both in classification and regression. In future work, one might further explore the potential of features that carry graph structure information empirically, and analyze more datasets in the context of graph-level tasks.

APPENDIX A

A.1 Supplemental Definitions for Sec. 5

Here, we provide additional definitions and notations.

Definition 4 (Node Discriminability). Let \mathbf{X} be a node feature matrix, and let $\mathbf{Y} = F(\mathbf{X})$ for some graph filter $F : \mathbb{R}^{n \times d_x} \rightarrow \mathbb{R}^{n \times d_y}$. We say that F discriminates two nodes $v, w \in V$ based on \mathbf{X} if $\mathbf{Y}[v] \neq \mathbf{Y}[w]$.

Definition 5 (K-step Neighborhood). For $K \in \mathbb{N}_0$,⁶ we define the K -step neighborhood of v as $\mathcal{N}_v^K := \{u \in V : 1 \leq d(u, v) \leq K\}$ (in particular $\mathcal{N}_v^0 = \emptyset$ and $\mathcal{N}_v^1 = \mathcal{N}_v$). We further write $\mathcal{N}_v^K := \mathcal{N}_v^K \cup \{v\}$ (in particular $\mathcal{N}_v^0 = \{v\}$).

Definition 6 (Induced Subgraph). Given a set $V_S \subseteq V$, we refer to a subgraph $S = (V_S, E_S)$ of G as an *induced subgraph*, if $E_S \subset E$ is the set of all edges that connect nodes from V_S , i.e., $E_S = E(V_S) := \{e \in E : e = \{v, w\} \in V_S \times V_S\}$. In this case, we will write $S := G(V_S)$.

Definition 7 (Graph Isomorphism). A *graph isomorphism* between graphs $G = (V, E)$ and $G' = (V', E')$ is a bijection $\phi : V \rightarrow V'$ such that $\{v, w\} \in E$ if and only if $\{\phi(v), \phi(w)\} \in E'$. We say that G and G' are ϕ -isomorphic and write $G \cong^\phi G'$. We also define $\phi(A) := \{\phi(w) : w \in A\}$ for $A \subset V$.

Definition 8 (Boundary and Interior of Induced Subgraph). Let $S = (V_S, E_S)$ be an induced subgraph of $G = (V, E)$. We define the *boundary* of S as $\partial S := \{w \in V_S : d(w, V \setminus V_S) = 1\}$. Further, we define the *interior* of S as $\text{int}(S) := V_S \setminus \partial S \subset V_S$. When convenient, we will also use the notation $\partial V_S := \partial S$ and $\text{int}(V_S) := \text{int}(S)$.

⁶ We use the conventions $\mathbb{N} := \{1, 2, 3, \dots\}$, $\mathbb{N}_0 := \mathbb{N} \cup \{0\}$ and $\mathbb{N}_{\geq k} := \{n \in \mathbb{N} : n \geq k\}$, for $k \in \mathbb{N}$.

Definition 9 (Spatial Support of Graph Filter). We say that a graph filter F has *spatial support* $L \in \mathbb{N}_0$ if the value of $F(\mathbf{X})[v]$ depends only on values of \mathbf{X} at nodes within L steps of v , i.e., if for any $v \in V$ and any node feature matrices \mathbf{X}_1 and \mathbf{X}_2 , we have $F(\mathbf{X}_1)[v] = F(\mathbf{X}_2)[v]$ whenever $\mathbf{X}_1[w] = \mathbf{X}_2[w]$ for all $w \in \mathcal{N}_v^L$.

A.2 Proof of Theorem 1

We use induction to show that $\mathbf{X}^\ell[u] = \mathbf{X}^\ell[\phi(u)]$ for all $u \in \mathcal{N}_v^{L-\ell}$ and all $0 \leq \ell \leq L$.

$\ell = 0$: Let $u \in \mathcal{N}_v^L$. By definition, we have $d(u, v) \leq L$, and so the triangle inequality implies that $\mathcal{N}_u^K \subseteq \mathcal{N}_v^{K+L}$. This implies that $G(\mathcal{N}_u^K) \cong^\phi G(\mathcal{N}_{\phi(u)}^K)$ and therefore the assumption that \mathbf{X} is K -intrinsic implies that $\mathbf{X}^0[u] = \mathbf{X}^0[\phi(u)]$.

$\ell \rightarrow \ell + 1$: By the inductive assumption we have that $\mathbf{X}^\ell[u] = \mathbf{X}^\ell[\phi(u)]$ for all $u \in \mathcal{N}_v^{L-\ell}$. Therefore, multiplying both sides by Θ^ℓ implies

$$\mathbf{X}_a^{\ell+1}[u] = \mathbf{X}^\ell[u] \Theta^\ell = \mathbf{X}^\ell[\phi(u)] \Theta^\ell = \mathbf{X}_a^{\ell+1}[\phi(u)] \quad (21)$$

for all $u \in \mathcal{N}_v^{L-\ell}$, where $\mathbf{X}_a^{\ell+1}$ is defined as in Eq. 6a. Now, if u is any element of $\mathcal{N}_v^{L-(\ell+1)}$ and w is any element of \mathcal{N}_u , the triangle inequality implies that $w \in \mathcal{N}_v^{L-\ell}$. Moreover, since degree is one-intrinsic and $K \geq 1$, we have that $d_u = d_{\phi(u)}$ and $d_w = d_{\phi(w)}$. Therefore, by Eq. 21,

$$\begin{aligned} \mathbf{X}_b^{\ell+1}[u] &= \sum_{w \in \mathcal{N}_u} \frac{1}{\sqrt{(d_u + 1)(d_w + 1)}} \mathbf{X}_a^{\ell+1}[w] \\ &= \sum_{w \in \mathcal{N}_u} \frac{1}{\sqrt{(d_{\phi(u)} + 1)(d_{\phi(w)} + 1)}} \mathbf{X}_a^{\ell+1}[\phi(w)] \\ &= \sum_{w' \in \mathcal{N}_{\phi(u)}} \frac{1}{\sqrt{(d_{\phi(u)} + 1)(d_{w'} + 1)}} \mathbf{X}_a^{\ell+1}[w'] \\ &= \mathbf{X}_b^{\ell+1}[\phi(u)] \end{aligned}$$

for all $u \in \mathcal{N}_v^{L-(\ell+1)}$, where $\mathbf{X}_b^{\ell+1}$ is defined as in Eq. 6b. Therefore, we have

$$\begin{aligned} \mathbf{X}^{\ell+1}[u] &= \mathbf{X}_c^{\ell+1}[u] = \sigma(\mathbf{X}_b^{\ell+1}[u]) \\ &= \sigma(\mathbf{X}_b^{\ell+1}[\phi(u)]) = \mathbf{X}_c^{\ell+1}[\phi(u)] = \mathbf{X}^{\ell+1}[\phi(u)] \end{aligned}$$

for all $u \in \mathcal{N}_v^{L-(\ell+1)}$ as desired. \square

A.3 Proof of Lemma 1

We will proceed by induction over j .

$j = 0$: Using the notation established in Notation 1, we have that $\tilde{U}_0 = V_{\text{diff}}^{\tilde{d}}$ and as noted in (i), this is exactly the set of nodes in $\mathcal{N}_v^{\tilde{d}}$ where a structural difference manifests. Thus the lemma holds or $j = 0$.

$j \rightarrow j + 1$: Assume Lemma 1 to hold for some $0 \leq j < \tilde{d}$. We need to show that the nodes in \tilde{U}_{j+1} are exactly the nodes in $\mathcal{N}_v^{\tilde{d}-(j+1)}$, where a structural difference is manifested relative to ϕ and the transformed node features

$\mathbf{Y}^{j+1} = \mathbf{P}^{j+1} \tilde{\mathbf{X}}$. We first note that for all $w \in \mathcal{N}_v^{\tilde{d}-(j+1)}$, we have that $d_w = d_{\phi(w)}$ since the degree of a vertex is 1-intrinsic and $\mathcal{N}_w \subseteq \mathcal{N}_v^{\tilde{d}-j} \subseteq \mathcal{N}_v^{\tilde{D}}$. Thus, by the definition of structural difference, our claim is equivalent to showing

$$\mathbf{Y}^{j+1}[u] \neq \mathbf{Y}^{j+1}[\phi(u)], \quad (22)$$

for all $u \in \tilde{U}_{j+1}$ and

$$\mathbf{Y}^{j+1}[w] = \mathbf{Y}^{j+1}[\phi(w)], \quad (23)$$

for all $w \in \mathcal{N}_v^{\tilde{d}-(j+1)} \setminus \tilde{U}_{j+1}$. Since $\mathbf{P}^{j+1} \tilde{\mathbf{X}} = \mathbf{P} \mathbf{P}^j \tilde{\mathbf{X}} = \mathbf{P} \mathbf{Y}^j$, we may use Eq. 8 to see that Eq. 22 is equivalent to

$$\begin{aligned} \frac{1}{2} \mathbf{Y}^j[u] + \frac{1}{2} \sum_{w \in \mathcal{N}_u} d_w^{-1} \mathbf{Y}^j[w] \\ \neq \frac{1}{2} \mathbf{Y}^j[\phi(u)] + \frac{1}{2} \sum_{w \in \mathcal{N}_{\phi(u)}} d_w^{-1} \mathbf{Y}^j[w] \end{aligned} \quad (24)$$

for every $u \in \tilde{U}_{j+1} \subseteq \mathcal{N}_v^{\tilde{d}-j}$. One may check that $\tilde{U}_{j+1} \cap \tilde{U}_j = \emptyset$, therefore we inductively apply Eq. 23 (with j in place of $j + 1$) to see that Eq. 24 is equivalent to

$$\sum_{w \in \mathcal{N}_u} d_w^{-1} \mathbf{Y}^j[w] \neq \sum_{w \in \mathcal{N}_{\phi(u)}} d_w^{-1} \mathbf{Y}^j[w]. \quad (25)$$

Similarly, $\mathbf{Y}^j[w] = \mathbf{Y}^j[\phi(w)]$ for all $w \in \mathcal{N}_u \setminus \tilde{U}_j$, Eq. 25 is equivalent to

$$\sum_{w \in \mathcal{N}_u \cap \tilde{U}_j} d_w^{-1} \mathbf{Y}^j[w] \neq \sum_{w \in \mathcal{N}_{\phi(u)} \cap \tilde{U}_j} d_w^{-1} \mathbf{Y}^j[w]. \quad (26)$$

The inductive hypothesis implies that Δ_u as defined in Definition 3 is equal to $\mathcal{N}_u \cap \tilde{U}_j$. Therefore, Eq. 26 follows from the assumption that $\text{int}(\mathcal{N}_v^{\tilde{d}})$ is not subject to coincidental correspondence. This completes the proof of Eq. 22.

Similarly Eq. 23. is equivalent to showing

$$\begin{aligned} \frac{1}{2} \mathbf{Y}^j[w] + \frac{1}{2} \sum_{\tilde{w} \in \mathcal{N}_w} d_{\tilde{w}}^{-1} \mathbf{Y}^j[\tilde{w}] \\ = \frac{1}{2} \mathbf{Y}^j[\phi(w)] + \frac{1}{2} \sum_{\tilde{w} \in \mathcal{N}_{\phi(w)}} d_{\tilde{w}}^{-1} \mathbf{Y}^j[\tilde{w}], \end{aligned} \quad (27)$$

for all $w \in \mathcal{N}_v^{\tilde{d}-(j+1)} \setminus \tilde{U}_{j+1}$. We first note that $\mathcal{N}_w \subseteq \mathcal{N}_v^{\tilde{d}-j}$, and that $w \notin \tilde{U}_j$, since otherwise we would have $d(\tilde{v}, w) = \tilde{d} - j > \tilde{d} - (j + 1)$. Therefore, the inductive hypothesis implies $\mathbf{Y}^j[w] = \mathbf{Y}^j[\phi(w)]$. Moreover, no $\tilde{w} \in \mathcal{N}_w$ can be an element of \tilde{U}_j since otherwise, w would be an element of \tilde{U}_{j+1} , which is a contradiction. Therefore, the inductive assumption implies $\mathbf{Y}^j[\tilde{w}] = \mathbf{Y}^j[\phi(\tilde{w})]$ for all $\tilde{w} \in \mathcal{N}_w$. We have already noted that $d_w = d_{\phi(w)}$ for all $w \in \text{int}(\mathcal{N}_v^{\tilde{D}})$. Thus, Eq. 27 holds and the proof is complete. \square

A.4 Proof of Theorem 2

We need to show that we can choose the parameters in a way that guarantees $F_{p\text{-sct}}(\mathbf{X})[v] \neq F_{p\text{-sct}}(\mathbf{X})[\phi(v)]$. For simplicity, we set $\Theta = \mathbf{I}_n$. In this case, since σ strictly monotonic, and therefore injective, it suffices to show that we can construct p such that

$$\mathbf{U}_p(\mathbf{X})[v] \neq \mathbf{U}_p(\mathbf{X})[\phi(v)]. \quad (28)$$

Using binary expansion, we may choose $k_1, \dots, k_m \in \mathbb{N}_0$, $k_i < k_{i+1}$, such that $d = 2^{k_1} + \dots + 2^{k_m}$. We will show that Eq. 28 holds for $p := (k_1, \dots, k_m)$. For $1 \leq i \leq m$, let $p_{:i} := (k_1, \dots, k_i)$ and let $t_i = \sum_{j=1}^i 2^{k_j}$, where $p_{:0}$ denotes the empty path of length 0 and $t_0 = 0$.

Recall the generalized path $P = (U_0, \dots, U_d)$ defined in Notation 1. We will use induction to show that, for $0 \leq i \leq m$, U_{t_i} is equal to the set of nodes in $\mathcal{N}_v^{d-t_i}$ such that a structural difference is manifested relative to ϕ and $\mathbf{Z}^i := \mathbf{U}_{p_{:i}} \mathbf{X}$. Since $t_m = d$ and $p_{:m} = p$, this claim will imply Eq. 28 and thus prove the theorem.

$i = 0$: Analogous to the proof of Lemma 1, using the notation established in Notation 1, we have that $U_0 = V_{\text{diff}}^d$, and as noted in the second bullet point, this is exactly the set of nodes in \mathcal{N}_v^d where a structural difference manifests. Thus the claim holds for $i = 0$.

$i \rightarrow i+1$: We now assume the result holds for i . Since the degree is one-intrinsic and $t_{i+1} \geq 1$, we have that $d_{\tilde{v}} = d_{\phi(\tilde{v})}$ for all $\tilde{v} \in \mathcal{N}_v^{d-t_{i+1}}$. Therefore, the claim is equivalent to showing

$$\mathbf{Z}^{i+1}[u] \neq \mathbf{Z}^{i+1}[\phi(u)], \quad (29)$$

for all $u \in U_{t_{i+1}}$ and

$$\mathbf{Z}^{i+1}[w] = \mathbf{Z}^{i+1}[\phi(w)], \quad (30)$$

for all $w \in \mathcal{N}_v^{d-t_{i+1}} \setminus U_{t_{i+1}}$.

By the inductive assumption, Eq.s 29 and 30 hold with i in place of $i+1$ and since σ is injective, they continue to hold when \mathbf{Z}^i is replaced with $\sigma(\mathbf{Z}^i)$. Therefore, we may apply Lemma 1 with $\sigma(\mathbf{Z}^i)$ in place of $\tilde{\mathbf{X}}$, and $j = 2^{k_{i+1}}$. By the inductive assumption, we have that \tilde{d} as defined in Lemma 1 is given by $\tilde{d} = d - t_i$. Therefore, $\tilde{d} - j = d - t_i - 2^{k_{i+1}} = d - t_{i+1}$ and $\tilde{U}_j = U_{t_{i+1}}$. Therefore, if $u \in U_{t_{i+1}}$ and $w \in \mathcal{N}_v^{d-t_{i+1}} \setminus U_{t_{i+1}}$, then a structural difference is manifested at u , but no structural difference is manifested at w . As noted above, $d_u = d_{\phi(u)}$. Therefore,

$$\mathbf{P}^{2^{k_{i+1}}} \sigma(\mathbf{Z}^i[u]) \neq \mathbf{P}^{2^{k_{i+1}}} \sigma(\mathbf{Z}^i[\phi(u)]) \quad (31)$$

and

$$\mathbf{P}^{2^{k_{i+1}}} \sigma(\mathbf{Z}^i[w]) = \mathbf{P}^{2^{k_{i+1}}} \sigma(\mathbf{Z}^i[\phi(w)]). \quad (32)$$

Next, we again apply Lemma 1 with $\sigma(\mathbf{Z}^i)$ in place of $\tilde{\mathbf{X}}$, but this time with $j = 2^{k_{i+1}-1}$. We observe now that $\tilde{d} - j = d - t_i - 2^{k_{i+1}-1} > d - t_{i+1}$ and thus $u, w \in \mathcal{N}_v^{\tilde{d}-j} \setminus \tilde{U}_j$. Therefore, as no structural difference is manifested at either u or w , we have that

$$\mathbf{P}^{2^{k_{i+1}-1}} \sigma(\mathbf{Z}^i[u]) = \mathbf{P}^{2^{k_{i+1}-1}} \sigma(\mathbf{Z}^i[\phi(u)]) \quad (33)$$

and

$$\mathbf{P}^{2^{k_{i+1}-1}} \sigma(\mathbf{Z}^i[w]) = \mathbf{P}^{2^{k_{i+1}-1}} \sigma(\mathbf{Z}^i[\phi(w)]). \quad (34)$$

Together Eq. 31-32 and Eq. 33-34 imply

$$\Psi_{k_{i+1}} \sigma(\mathbf{Z}^i[u]) \neq \Psi_{k_{i+1}} \sigma(\mathbf{Z}^i[\phi(u)])$$

and

$$\Psi_{k_{i+1}} \sigma(\mathbf{Z}^i[w]) = \Psi_{k_{i+1}} \sigma(\mathbf{Z}^i[\phi(w)]).$$

Eq. 29 and 30 now follow as $\mathbf{Z}^{i+1} = \Psi_{k_{i+1}} \sigma(\mathbf{Z}^i)$. \square

A.5 Modified Variant of Theorem 2

Theorem 3. *Similar to Theorem 2, let $\phi : V \rightarrow V$, $v \in V$ and $K, L \in \mathbb{N}$ such that $G(\mathcal{N}_v^{K+L}) \cong_{\phi} G(\mathcal{N}_{\phi(v)}^{K+L})$, and consider any K -intrinsic node feature matrix \mathbf{X} . Suppose there exist nodes $U \subset \mathcal{N}_v^{K+L}$ where a structural difference rel. to ϕ and \mathbf{X} is manifested. If the nonlinearity σ is strictly monotonic and there exists a unique $u \in U$ with minimal distance from v and a unique shortest path between them, we can define a scattering configuration (p, Θ) such that scattering features $F_{p\text{-scat}}(\mathbf{X})$ defined as in Eq. 12 discriminate v and $\phi(v)$.*

In Theorem 3, we replace the assumption of no coincidental correspondence (Definition 3) in Theorem 2 by the assumption of a unique shortest path between v and some node u , which is the unique nearest node from v , where a structural difference is manifested. The proof of Theorem 3 is based on the following auxiliary result.

Lemma 2. *Consider Δ_u as defined in Definition 3 and a feature matrix \mathbf{X} . If $|\Delta_u| = 1$, then u is not subject to coincidental correspondence with respect to ϕ and \mathbf{X} .*

Proof. For the sake of a contradiction, assume that $|\Delta_u| = 1$, but u is subject to coincidental correspondence. Letting w be the unique element of Δ_u , Eq. 19 simplifies to

$$d_w^{-1} \mathbf{X}[w] = d_{\phi(w)}^{-1} \mathbf{X}[\phi(w)],$$

which is equivalent to

$$d_{\phi(w)} \mathbf{X}[w] = d_w \mathbf{X}[\phi(w)]. \quad (35)$$

However, Eq. 35 cannot hold because we have that $w \in \Delta_u$ and therefore, by definition, a structural difference must manifest at w (see the footnote after Definition 2). \square

Proof of Theorem 3. The only difference between Theorem 3 and Theorem 2 is that in Theorem 2 we assume that there is no coincidental correspondence whereas here we assume that there is a unique $u \in U$ with minimal distance from v and that there is a unique shortest path between v and u . Inspecting the proof, we see that the only spot where we used the assumption of no coincidental correspondence was when we invoked Lemma 1. Therefore, it suffices to show that the conclusion of Lemma 1 holds under our revised assumptions. Moreover, inspecting the proof of Lemma 1, we see that the only spot we use the assumption of no coincidental correspondence was to establish Eq. 26. Thus, it suffices to show that Eq. 26 holds under our revised assumptions.

Let $P := (U_0, U_1, \dots, U_d)$ be the generalized path from u to v as defined in Notation 1, and note that our assumption of a unique shortest path implies that each U_j consists of a single node u_j . Since the assumption of no coincidental correspondence is not used in the base case, it suffices to assume that u_j is the unique element of \mathcal{N}_v^{d-j} where a structural difference manifests with respect to \mathbf{Y}^j and show that this implies that Eq. 26 holds for $j+1$. Let $\Delta_{u_{j+1}}$ be the set defined in Definition 3 with respect to feature matrix \mathbf{Y}^{j+1} . By the observation immediately following Eq. 26, we have $\Delta_{u_{j+1}} = \mathcal{N}_{u_j} \cap \tilde{U}_j = \{u_j\}$ and therefore $|\Delta_{u_{j+1}}| = 1$. Thus, Lemma 2 implies that u_{j+1} is not subject to coincidental correspondence with respect to ϕ and \mathbf{Y}^{j+1} .

TABLE 6
Chosen hyperparameters for our Sc-GCN model on the examined datasets.

	α	q	Scat. config.:		Channel widths:				
			U_{p_1}	U_{p_2}	A^1	A^2	A^3	U_{p_1}	U_{p_2}
<i>Citeseer</i>	0.50	4	Ψ_2	$\Psi_2 \Psi_3$	10	10	10	9	30
<i>Cora</i>	0.35	4	Ψ_1	Ψ_3	10	10	10	11	6
<i>Pubmed</i>	1.00	4	Ψ_1	Ψ_2	10	10	10	13	14
<i>DBLP (1st layer)</i>	1.00	4	Ψ_1	Ψ_2	10	10	10	30	30
<i>DBLP (2nd layer)</i>	0.10	1	Ψ_1	Ψ_2	40	20	20	20	20

This in turn, implies that Eq. 26 holds and thus completes the proof. \square

APPENDIX B

B.1 Technical Details

As with most neural networks, when implementing Sc-GCN and GSAN, one must make several architecture choices and tune several hyperparameters. In our experiments with Sc-GCN, we used either one or two hybrid layers, each comprised of three GCN channels and two scattering channels, followed by a single residual convolution layer. This fairly simple setup simplified the network tuning process and was sufficient to obtain strong results, which outperformed numerous competing methods. However, it is likely that performance can be further improved by using wider or deeper networks. For *Cora*, *Citeseer* and *Pubmed* we used only one hybrid layer as preliminary experiments indicated that the addition of a second one was not cost-effective (in light of additional complexity created by the need to tune more hyperparameters). For *DBLP*, two layers were used due to a significant increase in performance. We note that even with a single hybrid layer our model achieves 73.1% test accuracy (compared to the reported 81.5% for two layers) and still significantly outperforms GAT (66.1%) and the other methods (below 60%).

Validation & testing procedure: All tests were done using train-validation-test splits of the datasets. We used the validation accuracy to tune the hyperparameters and reported the test accuracy in the comparison tables. To ensure fair comparison, we used the same splits for all methods. On *Citeseer*, *Cora* and *Pubmed*, we used the same settings as in [5], and followed the standard practices used in other works which have used these datasets. For *DBLP*, as far as we know, no common standard is established in the literature. Here, we used a ratio of 5 : 1 : 1 between

train, validation, and test for all node-classification datasets. For the datasets for graph classification and regression, we used a ratio of 8 : 1 : 1.

Hyperparameter tuning: We tuned our hyperparameters on each set using a grid search and selected the setting which yields the highest accuracy on the validation set.

In Sc-GCN, we used the grid search to tune the parameter α used in the residual convolution, the exponent q used in the nonlinearity, the scattering channel configurations p_1, p_2 (i.e., scales used in these two channels), and the widths of channels in the network, i.e. the hidden dimensions. The results of this tuning process are presented in Tab. 6. We note that for *DBLP*, the hybrid-layer parameters are shared between the two layers in order to simplify the tuning process. This was generally less exhaustive than the process used for the other three datasets, since our method significantly outperformed all other methods even with limited tuning.

For GSAN, the hyperparameter selection is less intricate, which in addition to improved performance, is one of the main advantages compared to Sc-GCN. In particular, we use the same scattering configurations and channel widths across all channels in a given layer. We do not tune the scattering configurations. We always set $m = 1$ and always use the wavelets Ψ_1, Ψ_2 , and Ψ_3 in our three scattering channels. Therefore, the hyperparameters simplify to α , a (universal) channel width and the number of attention heads. These parameters might differ across different layers if the architecture relies on several ones. The results of this tuning process are presented in Tab. 7.

Hardware & software environment: All experiments were done on the same HPC cluster with intel i7-6850K CPU and NVIDIA TITAN X Pascal GPU. Both Sc-GCN and GSAN were implemented using PyTorch [50]. Implementations of all other methods were taken directly from the code accompanying their publications.

TABLE 7
Chosen hyperparameters for our GSAN model on the examined datasets.

	α	Number of heads	Channel width
<i>Texas</i>	1.5	4	128
<i>Chameleon</i>	0.2	64	32
<i>CoraFull</i>	0.5	20	128
<i>Wiki-CS</i>	0.3	20	20
<i>Citeseer</i>	0.1	8	64
<i>Pubmed</i>	0.1	50	64
<i>Cora</i>	0.1	50	64
<i>DBLP</i>	0.2	16	128

B.2 Ablation Study

The two primary novelties in Sc-GCN are the scattering channels (i.e., U_{p_1} and U_{p_2}) and the residual convolution (controlled by the hyperparameter α). To explore their contribution and the dependence of the network performance on the hyperparameters, Tab. 8-12 show classification results over the Cora dataset for $\alpha = 0.01, 0.1, 0.35, 0.5, 1.0$ over multiple scattering channel configurations. For simplicity, we focus on *Cora*, but note that similar results are observed on the other datasets. The rows and columns in each table denote the two scattering channels used in the Sc-GCN, together with the three GCN channels (i.e., A^{r_k} , $r_k = 1, 2, 3$).

TABLE 8
Classification accuracies on Cora with $\alpha = 0.01$ with average accuracy 80.4% over all scales.

ACCURACY	Ψ_1	Ψ_2	Ψ_3	$\Psi_2 \Psi_3$	$\Psi_1 \Psi_2$
Ψ_1	0.808	0.808	0.805	0.806	0.806
Ψ_2	0.809	0.809	0.806	0.806	0.806
Ψ_3	0.802	0.804	0.801	0.801	0.800
$\Psi_2 \Psi_3$	0.802	0.804	0.801	0.800	0.799
$\Psi_1 \Psi_2$	0.802	0.804	0.801	0.800	0.800

TABLE 9
Classification accuracies on Cora with $\alpha = 0.1$ with average accuracy 80.9% over all scales.

ACCURACY	Ψ_1	Ψ_2	Ψ_3	$\Psi_2 \Psi_3$	$\Psi_1 \Psi_2$
Ψ_1	0.813	0.813	0.812	0.808	0.809
Ψ_2	0.817	0.817	0.810	0.810	0.815
Ψ_3	0.810	0.808	0.801	0.800	0.806
$\Psi_2 \Psi_3$	0.812	0.811	0.801	0.800	0.809
$\Psi_1 \Psi_2$	0.813	0.811	0.802	0.802	0.809

TABLE 10
Classification accuracies on Cora with $\alpha = 0.35$ with average accuracy 83.5%.

ACCURACY	Ψ_1	Ψ_2	Ψ_3	$\Psi_2 \Psi_3$	$\Psi_1 \Psi_2$
Ψ_1	0.838	0.836	0.835	0.837	0.837
Ψ_2	0.842	0.836	0.835	0.838	0.837
Ψ_3	0.835	0.836	0.833	0.833	0.832
$\Psi_2 \Psi_3$	0.835	0.836	0.833	0.833	0.831
$\Psi_1 \Psi_2$	0.835	0.836	0.832	0.833	0.831

TABLE 11
Classification accuracies on Cora with $\alpha = 0.5$ with average accuracy 82.7% over all scales.

ACCURACY	Ψ_1	Ψ_2	Ψ_3	$\Psi_2 \Psi_3$	$\Psi_1 \Psi_2$
Ψ_1	0.828	0.828	0.836	0.836	0.835
Ψ_2	0.828	0.833	0.830	0.830	0.827
Ψ_3	0.821	0.829	0.826	0.826	0.826
$\Psi_2 \Psi_3$	0.820	0.828	0.826	0.825	0.825
$\Psi_1 \Psi_2$	0.821	0.829	0.824	0.824	0.824

TABLE 12
Classification accuracies on Cora with $\alpha = 1.0$ with average accuracy 82.3% over all scales.

ACCURACY	Ψ_1	Ψ_2	Ψ_3	$\Psi_2 \Psi_3$	$\Psi_1 \Psi_2$
Ψ_1	0.817	0.818	0.827	0.827	0.824
Ψ_2	0.820	0.819	0.824	0.824	0.823
Ψ_3	0.826	0.823	0.823	0.823	0.821
$\Psi_2 \Psi_3$	0.825	0.823	0.823	0.823	0.821
$\Psi_1 \Psi_2$	0.822	0.823	0.823	0.823	0.821

TABLE 13

Impact of removing each individual channel from the optimal configuration on Cora, while classifying using the remaining four channels. Full Sc-GCN accuracy provided for reference.

Removed Channel	A	A^2	A^3	Ψ_2	Ψ_1	None
Accuracy	82.0	80.7	80.9	83.7	82.7	84.2

To examine the importance of the parameter α used in the residual graph convolution layer, we observe that setting $\alpha = 0$ effectively eliminates this layer (since then $A_{\text{res}} = I_n$). On the other hand, increasing α makes the filtering effect stronger, approaching a random-walk filtering as $\alpha \rightarrow \infty$. We evaluate the effect of this parameter on classification accuracy. Our results, displayed in Tab. 8-12 indicate that increasing α to non-negligible nonzero values improves classification performance, which we interpret to be due to the removal of high-frequency noise. However, when α further increases (in particular when $\alpha = 1$ in this case) the smoothing provided by this layer degrades the performance to a level close to the traditional GCN [5].

We next consider the scales used in the two scattering channels of our hybrid architecture, which correspond to the rows and columns of Tab. 8-12 here. Our results show that the network is relatively robust to the choice of scales. However, we generally observe that utilizing purely second-order coefficients gives slightly worse results than using either purely first-order coefficients or a mix of first- and second-order coefficients. That said, most configurations of scattering scales (with properly-tuned α) give better results than pure GCN.

We note that for $\alpha = 0.35$ (Tab. 10), all scale configurations outperform GAT (83%) and all other reported methods in Tab. 2. We also note that the graph residual convolution is only useful because of the presence of the scattering channels. By itself, the residual convolution layer only applies a low-pass (smoothing) filter and therefore, would essentially be equivalent to a conventional GCN without scattering channels.

Finally, to examine the relative importance of the low-pass and band-pass information, we provide an ablation study of the impact each channel. We focus on the Cora dataset, set $\alpha = 0.35$ and use the best channel configuration, which achieved 84.2% accuracy when all channels were used. Then, we remove each of the band-pass or low-pass channels individually from the network, and reevaluate network performance with the remaining four channels. Our results are displayed in Tab. 13. They indicate that the information captured by both the band-pass and the low-pass channels is important and that eliminating either decreases performance. In particular, we note that eliminating Ψ_1 has a major impact on the accuracy, since without it, Sc-GCN will not outperform GAT.

B.3 Implementation

Python code accompanying this work is available on github.com/dms-net/scatteringGCN and github.com/dms-net/Attention-based-Scattering

ACKNOWLEDGMENTS

The authors would like to thank Dongmian Zou for fruitful discussions. This work was partially funded by Fin-ML CREATE graduate studies scholarship for PhD [F.W.]; IVADO (Institut de valorisation des données) grant PRF-2019-3583139727, FRQNT (Fonds de recherche du Québec - Nature et technologies) grant 299376, Canada CIFAR AI Chair [G.W.]; NSF (National Science Foundation) grant DMS-1845856 [M.H.]; and NIH (National Institutes of Health) grant NIGMS-R01GM135929 [M.H.,G.W.]. The content provided here is solely the responsibility of the authors and does not necessarily represent the official views of the funding agencies.

REFERENCES

- [1] M. M. Bronstein, J. Bruna, Y. LeCun, A. Szlam, and P. Vandergheynst, "Geometric deep learning: going beyond euclidean data," *IEEE Signal Processing Magazine*, vol. 34, no. 4, pp. 18–42, 2017.
- [2] M. M. Bronstein, J. Bruna, T. Cohen, and P. Veličković, "Geometric deep learning: Grids, groups, graphs, geodesics, and gauges," *arXiv preprint arXiv:2104.13478*, 2021.
- [3] J. Gilmer, S. S. Schoenholz, P. F. Riley, O. Vinyals, and G. E. Dahl, "Neural message passing for quantum chemistry," in *International conference on machine learning*. PMLR, 2017, pp. 1263–1272.
- [4] W. L. Hamilton, R. Ying, and J. Leskovec, "Inductive representation learning on large graphs," in *Proceedings of the 31st International Conference on Neural Information Processing Systems*, 2017, pp. 1025–1035.
- [5] T. N. Kipf and M. Welling, "Semi-supervised classification with graph convolutional networks," in the *4th International Conference on Learning Representations (ICLR)*, 2016.
- [6] A. M. Fout, "Protein interface prediction using graph convolutional networks," Ph.D. dissertation, Colorado State University, 2017.
- [7] N. De Cao and T. Kipf, "Molgan: An implicit generative model for small molecular graphs," *arXiv preprint arXiv:1805.11973*, 2018.
- [8] B. Knyazev, X. Lin, M. R. Amer, and G. W. Taylor, "Spectral multigraph networks for discovering and fusing relationships in molecules," *arXiv preprint arXiv:1811.09595*, 2018.
- [9] Q. Li, Z. Han, and X.-M. Wu, "Deeper insights into graph convolutional networks for semi-supervised learning," in *Proceedings of the Thirty-Second AAAI Conference on Artificial Intelligence (AAAI-18)*. Association for the Advancement of Artificial Intelligence, 2018, pp. 3538–3545.
- [10] P. Veličković, G. Cucurull, A. Casanova, A. Romero, P. Liò, and Y. Bengio, "Graph attention networks," in *International Conference on Learning Representations*, 2018.
- [11] H. Nt and T. Maehara, "Revisiting graph neural networks: All we have is low-pass filters," *arXiv preprint arXiv:1905.09550*, 2019.
- [12] F. Gama, A. Ribeiro, and J. Bruna, "Diffusion scattering transforms on graphs," in *International Conference on Learning Representations*, 2019.
- [13] F. Gao, G. Wolf, and M. Hirn, "Geometric scattering for graph data analysis," in *Proceedings of the 36th International Conference on Machine Learning*, 2019, pp. 2122–2131.
- [14] D. Zou and G. Lerman, "Graph convolutional neural networks via scattering," *Applied and Computational Harmonic Analysis*, vol. 49, no. 3, pp. 1046–1074, 2020.
- [15] S. Mallat, "Group invariant scattering," *Communications on Pure and Applied Mathematics*, vol. 65, no. 10, pp. 1331–1398, 2012.
- [16] D. K. Hammond, P. Vandergheynst, and R. Gribonval, "Wavelets on graphs via spectral graph theory," *Applied and Computational Harmonic Analysis*, vol. 30, no. 2, pp. 129–150, 2011.
- [17] R. R. Coifman and M. Maggioni, "Diffusion wavelets," *Applied and computational harmonic analysis*, vol. 21, no. 1, pp. 53–94, 2006.
- [18] R. Liao, Z. Zhao, R. Urtasun, and R. Zemel, "Lanczosnet: Multi-scale deep graph convolutional networks," in the *7th International Conference on Learning Representations (ICLR)*, 2019.
- [19] S. Abu-El-Haija, B. Perozzi, A. Kapoor, N. Alipourfard, K. Lerman, H. Harutyunyan, G. Ver Steeg, and A. Galstyan, "Mixhop: Higher-order graph convolutional architectures via sparsified neighborhood mixing," in *international conference on machine learning*. PMLR, 2019, pp. 21–29.
- [20] B. Xu, H. Shen, Q. Cao, Y. Qiu, and X. Cheng, "Graph wavelet neural network," *arXiv preprint arXiv:1904.07785*, 2019.
- [21] F. Gama, A. Ribeiro, and J. Bruna, "Stability of graph scattering transforms," in *Advances in Neural Information Processing Systems*, 2019, pp. 8038–8048.
- [22] M. Perlmutter, F. Gao, G. Wolf, and M. Hirn, "Understanding graph neural networks with asymmetric geometric scattering transforms," *arXiv preprint arXiv:1911.06253*, 2019.
- [23] D. Zou and G. Lerman, "Encoding robust representation for graph generation," in *2019 International Joint Conference on Neural Networks (IJCNN)*. IEEE, 2019, pp. 1–9.
- [24] E. Castro, A. Benz, A. Tong, G. Wolf, and S. Krishnaswamy, "Uncovering the folding landscape of rna secondary structure using deep graph embeddings," in *2020 IEEE International Conference on Big Data (Big Data)*, 2020, pp. 4519–4528.
- [25] D. Bhaskar, J. D. Grady, M. A. Perlmutter, and S. Krishnaswamy, "Molecular graph generation via geometric scattering," *arXiv preprint arXiv:2110.06241*, 2021.
- [26] A. Tong, F. Wenkel, K. MacDonald, S. Krishnaswamy, and G. Wolf, "Data-driven learning of geometric scattering networks," *arXiv preprint arXiv:2010.02415*, 2020.
- [27] J. Bruna, W. Zaremba, A. Szlam, and Y. LeCun, "Spectral networks and deep locally connected networks on graphs," in *2nd International Conference on Learning Representations, ICLR 2014*, 2014.
- [28] M. Defferrard, X. Bresson, and P. Vandergheynst, "Convolutional neural networks on graphs with fast localized spectral filtering," in *Advances in Neural Information Processing Systems (NeurIPS)*, vol. 29, 2016, pp. 3844–3852.
- [29] R. Levie, W. Huang, L. Bucci, M. Bronstein, and G. Kutyniok, "Transferability of spectral graph convolutional neural networks," *Journal of Machine Learning Research*, vol. 22, no. 272, pp. 1–59, 2021.
- [30] A. Susnjara, N. Perraudin, D. Kressner, and P. Vandergheynst, "Accelerated filtering on graphs using Lanczos method," 2015, arXiv:1509.04537.
- [31] R. Levie, F. Monti, X. Bresson, and M. M. Bronstein, "Cayleynets: Graph convolutional neural networks with complex rational spectral filters," *IEEE Transactions on Signal Processing*, vol. 67, no. 1, pp. 97–109, 2018.
- [32] P. Barceló, E. V. Kostylev, M. Monet, J. Pérez, J. Reutter, and J. P. Silva, "The logical expressiveness of graph neural networks," in *International Conference on Learning Representations*, 2020.
- [33] Y. Min, F. Wenkel, and G. Wolf, "Scattering gcn: Overcoming oversmoothness in graph convolutional networks," *Advances in Neural Information Processing Systems*, vol. 33, 2020.
- [34] —, "Geometric scattering attention networks," in *ICASSP 2021-2021 IEEE International Conference on Acoustics, Speech and Signal Processing (ICASSP)*. IEEE, 2021, pp. 8518–8522.
- [35] P. Veličković, G. Cucurull, A. Casanova, A. Romero, P. Lio, and Y. Bengio, "Graph attention networks," in the *6th International Conference on Learning Representations (ICLR)*, 2018.
- [36] B. Rozemberczki, C. Allen, and R. Sarkar, "Multi-scale attributed node embedding," *Journal of Complex Networks*, vol. 9, no. 2, p. cnab014, 2021.
- [37] M. Rudelson, "Invertibility of random matrices: Norm of the inverse," *ANNALS OF MATHEMATICS*, 2008.
- [38] X. Zhu, Z. Ghahramani, and J. D. Lafferty, "Semi-supervised learning using gaussian fields and harmonic functions," in *Proceedings of the 20th International conference on Machine learning (ICML-03)*, 2003, pp. 912–919.
- [39] X.-M. Wu, Z. Li, A. M. So, J. Wright, and S. fu Chang, "Learning with partially absorbing random walks," in *Advances in Neural Information Processing Systems 25*, F. Pereira, C. J. C. Burges, L. Bottou, and K. Q. Weinberger, Eds., 2012, pp. 3077–3085.
- [40] Z. Yang, W. Cohen, and R. Salakhudinov, "Revisiting semi-supervised learning with graph embeddings," in *International conference on machine learning*. PMLR, 2016, pp. 40–48.
- [41] S. Pan, J. Wu, X. Zhu, C. Zhang, and Y. Wang, "Tri-party deep network representation," *Network*, vol. 11, no. 9, p. 12, 2016.
- [42] H. Pei, B. Wei, K. C.-C. Chang, Y. Lei, and B. Yang, "Geom-gcn: Geometric graph convolutional networks," *arXiv preprint arXiv:2002.05287*, 2020.

- [43] P. Mernyei and C. Cangea, "Wiki-cs: A wikipedia-based benchmark for graph neural networks," *arXiv preprint arXiv:2007.02901*, 2020.
- [44] A. Bojchevski and S. Günnemann, "Deep gaussian embedding of graphs: Unsupervised inductive learning via ranking," in *International Conference on Learning Representations*, 2018, pp. 1–13.
- [45] P. Yanardag and S. Vishwanathan, "Deep graph kernels," in *Proceedings of the 21th ACM SIGKDD international conference on knowledge discovery and data mining*, 2015, pp. 1365–1374.
- [46] O. Vinyals, S. Bengio, and M. Kudlur, "Order matters: Sequence to sequence for sets," *arXiv preprint arXiv:1511.06391*, 2015.
- [47] S. Hochreiter and J. Schmidhuber, "Long short-term memory," *Neural computation*, vol. 9, no. 8, pp. 1735–1780, 1997.
- [48] J. J. Irwin and B. K. Shoichet, "Zinc- a free database of commercially available compounds for virtual screening," *Journal of chemical information and modeling*, vol. 45, no. 1, pp. 177–182, 2005.
- [49] Z. Wu, B. Ramsundar, E. N. Feinberg, J. Gomes, C. Geniesse, A. S. Pappu, K. Leswing, and V. Pande, "Moleculenet: a benchmark for molecular machine learning," *Chemical science*, vol. 9, no. 2, pp. 513–530, 2018.
- [50] A. Paszke, S. Gross, F. Massa, A. Lerer, J. Bradbury, G. Chanan, T. Killeen, Z. Lin, N. Gimelshein, L. Antiga *et al.*, "Pytorch: An imperative style, high-performance deep learning library," *Advances in neural information processing systems*, vol. 32, pp. 8026–8037, 2019.



Frederik Wenkel received the B.Sc. degree in Mathematics and the M.Sc. degree in Mathematics at Technical University of Munich, in 2019. He is currently a Ph.D. candidate in Applied Mathematics at Université de Montréal (UdeM) and Mila (the Quebec AI institute), working on geometric deep learning. In particular, he is interested in graph neural networks and their applications in domains such as social networks, bio-chemistry and finance.



Yimeng Min is a Ph.D. student in Computer Science at Cornell University. He received his B.Sc. degree in Physics from Nanjing University and M.A.Sc. degree in Electrical and Computer Engineering from University of Toronto. His research area is Artificial Intelligence with a focus on graph neural networks and constraint reasoning.



Matthew Hirn is an Associate Professor in the Department of Computational Mathematics, Science & Engineering and the Department of Mathematics at Michigan State University. At Michigan State he is the scientific leader of the ComplEx Data Analysis Research (CEDAR) team, which develops new tools in computational harmonic analysis, machine learning, and data science for the analysis of complex, high dimensional data. Hirn received his B.A. in Mathematics from Cornell University and his Ph.D. in Mathematics from the University of Maryland, College Park. Before arriving at MSU, he held postdoctoral appointments in the Applied Math Program at Yale University and in the Department of Computer Science at Ecole Normale Supérieure, Paris. He is the recipient of the Alfred P. Sloan Fellowship (2016), the DARPA Young Faculty Award (2016), the DARPA Director's Fellowship (2018), and the NSF CAREER award (2019), and was designated a Kavli Fellow by the National Academy of Sciences (2017).



Michael Perlmutter Michael Perlmutter is a Hedrick Assistant Adjunct Professor in the Department of Mathematics at the University of California Los Angeles. Previously, he has held postdoctoral positions in the Department of Computational Mathematics, Science and Engineering at Michigan State University and in the Department of Statistics and Operations Research at the University of North Carolina at Chapel Hill. He earned his Ph.D. in mathematics from Purdue University in 2016. His research

uses the methods of applied probability and computational harmonic analysis to develop and analyze new methods for data sets with geometric structure.



Guy Wolf is an associate professor in the Department of Mathematics and Statistics (DMS) at the Université de Montréal (UdeM), a core academic member of Mila (the Quebec AI institute), and holds a Canada CIFAR AI Chair. He is also affiliated with the CRM center of mathematical sciences and the IVADO institute of data valorization. He holds an M.Sc. and a Ph.D. in computer science from Tel Aviv University. Prior to joining UdeM in 2018, he was a postdoctoral researcher (2013-2015) in the Department of

Computer Science at École Normale Supérieure in Paris (France), and a Gibbs Assistant Professor (2015-2018) in the Applied Mathematics Program at Yale University. His research focuses on manifold learning and geometric deep learning for exploratory data analysis, including methods for dimensionality reduction, visualization, denoising, data augmentation, and coarse graining. Further, he is particularly interested in biomedical data exploration applications of such methods, e.g., in single cell genomics/proteomics and neuroscience.